International Journal of Heat and Mass Transfer 223 (2024) 125238

Contents lists available at ScienceDirect

International Journal of Heat and Mass Transfer

journal homepage: www.elsevier.com/locate/ijhmt

# Heat transfer and evaporation processes from the Enskog-Vlasov equation and its moment equations

Henning Struchtrup [a,*], Hamidreza Jahandideh [a], Arthur Couteau [b], Aldo Frezzotti [c]

[a] Department of Mechanical Engineering, University of Victoria, PO Box 1700 STN CSC, Victoria, V8W 2Y2, British Columbia, Canada
[b] Swiss Federal Laboratories for Materials Science and Technology (Empa), Automotive Powertrain Technologies Laboratory, Dubendorf, CH-8600, Switzerland
[c] Dipartimento di Scienze e Tecnologie Aerospaziali, Politecnico di Milano, Via La Masa 34, Milano, 20156, Italy

ARTICLE INFO

*Keywords:*
Liquid-vapor interface
Evaporation and condensation
Nonequilibrium
Enskog-Vlasov equation
Moment equations

ABSTRACT

Nonequilibrium heat and mass transfer processes through liquid-vapor interfaces are studied through solutions of the Enskog-Vlasov (EV) equation and the corresponding system of EV26 moment equations. These models fully resolve liquid and vapor bulk regions and the diffuse interface connecting both. With that, evaporation and heat transfer processes can be studied without the need of modeled interface relations. Comparison of numerical results shows qualitative agreement of moment simulations with DSMC solutions of the EV equation, but quantitative differences. Interface resistivities for jump interface conditions are determined from the simulations, which show marked differences to those found from classical kinetic theory, where dimensionless resistivities are constants. In contrast, the EV models give temperature dependent resistivities, some negative off-diagonal resistivities, and indicate non-linear behavior where resistivities depend on mass and heat fluxes through the interface. In summary, the results point to the urgent need for systematic evaluation of resistivities over a wide range of conditions between weak and strong nonequilibrium, close to and far from the critical point.

## 1. Introduction

Evaporation and condensation processes in non-equilibrium, while ubiquitous in daily life and technical applications, are surprisingly little understood on a fundamental level. While from the macroscopic viewpoint the phase change occurs at a sharp interface between the phases, detailed microscopic modeling, e.g., with molecular dynamics (MD) [1–9], reveals that the phase change occurs in a diffuse interface with the width of $\sim 10-20$ molecular diameters.

In macroscopic models, the intricate processes in the diffuse interface are subsumed into a handful of coefficients [10–12], whose dependence on the state of the interface (such as temperature) and processes (such as magnitude of the evaporation mass flux) is still not well understood. For instance, measured values for condensation and evaporation coefficients of water vary over at least three orders of magnitude [13,14], which points to difficulty in both, measurements and modeling.

C.A. Ward and co-workers, in careful macroscopic measurements on the evaporation of water and other substances [15–20] observed temperature jumps of up to 7 °C between liquid and vapor directly at the interface, which points to interfacial resistivities being much larger than commonly assumed or, correspondingly, to evaporation and condensation coefficients significantly smaller than unity. Further experimental investigations of interfacial temperature jumps during the evaporation of water can be found in Refs. [21,22].

To shed detailed light on interfacial behavior, a wide array of microscopic simulations, covering the full range of process conditions from close to equilibrium to strong nonequilibrium, is required. Such simulations, which rely only on microscopic parameters that describe individual molecules and their interaction, resolve the diffuse interface and can be used to extract the phenomenological coefficients that appear in the sharp interface models required in macroscopic transport simulations.

While molecular dynamics (MD) appears to be the most accurate way to perform such simulations, it generally demands large computational times, in particular when the system exhibits small deviations from equilibrium, which are difficult to detect by any particles methods due to unfavorable signal to stochastic noise ratios.

In this contribution we explore a kinetic model derived from the Enskog-Vlasov (EV) equation [23,24], which is a generalization of the classical Enskog theory of the dense hard sphere fluid [25] to include inter-molecular attraction [26], not present in the purely repulsive hard

* Corresponding author.
*E-mail addresses:* struchtr@uvic.ca (H. Struchtrup), aldo.frezzotti@polimi.it (A. Frezzotti).

https://doi.org/10.1016/j.ijheatmasstransfer.2024.125238
Received 30 November 2023; Received in revised form 12 January 2024; Accepted 23 January 2024

spheres potential. With that, the model phenomenologically describes liquid and vapor phases as well as the resolved interfacial structure. In addition to the microscopic parameters defining the molecules and their interactions, the EV equation inherits from the Enskog theory the need to specify the pair correlation function [27,28], being based on the one-particle distribution function as its parent Boltzmann equation [29–32] which describes ideal gases.

The complexity of kinetic equations and, in particular, of the EV equation requires adopting numerical solution methods. Although not the only option at hand [33], a suitable extension [35,36] of the classical Direct Simulation Monte Carlo (DSMC) [37] provides a simple, convenient and easily extensible [38–40] tool to obtain approximate solutions of the EV equation.

Similar to MD simulations, solutions of the EV equation itself, by means of a particle method like DSMC, are computationally expensive, although not as expensive as MD simulations [35,36,41]. As for MD, computational costs increase considerably when flow conditions exhibit small deviations from equilibrium which are difficult to separate from the prevailing Maxwellian distribution function, due to the unfavorable signal to noise ratio.

An alternative is offered by a set of 26 moment equations (EV26 equations) recently derived as an approximation to the EV equation [42]. Unlike traditional diffuse interface models, based on Navier-Stokes-Fourier (NSF) constitutive laws [43], the EV26 model has the capability to describe the kinetic (Knudsen) layer next to the liquid-vapor interface, whose presence cannot be ignored [4,8].

Numerical solutions of the EV26 equations give deterministic solutions over a wide range of process conditions—from low to strong nonequilibrium—at low computational cost. Hence they promise a much quicker access to explore the full range of interfacial behavior. Before this is done, however, it is necessary to evaluate the EV26 equations for their accuracy, by comparing their predictions with results from the underlying kinetic equation itself, i.e., from DSMC solutions of the EV equation.

In the following, we present and critically discuss selected simulation results from EV-DSMC and EV-moment models. The results show that the EV moment models reproduce non-equilibrium features seen in the DSMC simulations, but overestimate the interfacial resistance. Extensions of the moment model to include elements of higher moment equations yield somewhat better results, and must be further explored in the future.

Further to this comparison, we use DSMC and moment results to determine resistivities, and shed new light on the interfacial behavior in non-equilibrium.

The remainder of the paper is structured as follows: In Sec. 2 we introduce the one-dimensional process geometry used for the simulations, followed by a short description of sharp interface models with interfacial resistivities in Sec. 3. Then, in Sec. 4, we introduce the Enskog-Vlasov equation [23,24], and briefly outline the derivation of its moment equations [42] by means of Grad's moment method [44,45,32,31]. The equations for 26 moments are shown already in reduced form for 1D steady state processes. Far from the interface the EV26 equations reduce to the equations of classical hydrodynamics, but in the interfacial region they exhibit a large number of additional terms that describe the local nonequilibrium state, including Knudsen layer effects. The EV equation itself, and its moment equations are solved numerically for heat transfer and evaporation problems, with numerical methods and discretization errors outlined in Sec. 5.

Subsequent sections present and discuss solutions for heat transfer and evaporation problems. The solutions fully resolve the nonequilibrium processes in the interfacial regions, where the higher moments obtained from EV-DSMC and EV26 solutions play an important role for the overall transport behavior. Comparison with between DSMC and moment solutions shows qualitative agreement of the EV26 equations for a wider range of conditions, but quantitative agreement only for conditions closer to the critical state. Addition of regularizing terms [46] somewhat improves the agreement, and indicates that further away from the critical point a larger number of moments will be required.

From the numerical solutions we extract the (dimensionless) resistivities for NSF, which show variation with interface temperature, being larger for colder interfaces. Moreover, in particular for processes involving evaporation, resistivities obtained from the moment equations vary with the evaporation rate, so much that the direction of temperature jumps can change sign. While the presented results are, of course, limited to the EV moment system, it appears likely that also other, more realistic, systems will behave in a similar fashion.

Our results indicate that full understanding of interfacial transport can only be reached by examining processes over a wide range of processes, from close to far from the critical point, and from weak to strong nonequilibrium.

The results presented below extend and refine preliminary work presented in the theses of two of the present authors [47,48].

## 2. One-dimensional steady state evaporation and condensation

In the following, we focus on one-dimensional steady state processes, with a plane interface separating a liquid region from a vapor region. Transport of mass and heat is normal to the interface, described by the coordinate $x$, and we chose a frame of reference where the interface is at rest.

Fig. 1 shows simple sketches for macroscopic and microscopic viewpoints with sharp and diffuse interfaces, respectively. Here, $J$ and $Q$ are the total mass and energy fluxes that are constant due to conservation of mass and energy. Moreover, the normal momentum flux $P$ is constant as well, which for sufficiently slow processes implies that both bulk phases are at the same pressure $p$, as indicated in the figure.

Under the prescribed restrictions, the conservation laws for mass, momentum and energy in the bulk liquid or vapor phases reduce to [10,12]

$$\begin{aligned} \rho v &= J = const \\ p &= P = const \\ \rho v h + q &= Q = const \end{aligned} \tag{1}$$

where $\rho$ denotes mass density, $v$ is flow velocity relative to the interface, $p(\rho,T)$ is pressure as given by the thermal equation of state, $h(\rho,T)$ is enthalpy as given by the caloric equation of state, and $q = -\kappa \frac{dT}{dx}$ is non-convective heat flux with heat conductivity $\kappa(\rho,T)$; $T$ denotes thermodynamic temperature. Note that due to the assumed low Mach numbers viscosity effects do not play a role.

These equations are derived under the assumption that the bulk phases are in local thermodynamic equilibrium, so that the classical hydrodynamic equations—the laws of Navier-Stokes and Fourier (NSF)—are valid.

For sharp interface models, NSF is considered for states arbitrarily close to the interface, while all nonequilibrium effects associated with phase change are pushed into the description of the interface.

Within the interfacial region of diffuse interfaces the NSF laws are not valid, and more elaborate models must be used to describe the strong deviations from local equilibrium in a wider region around the interface, where the nonequilibrium effects occur. This region includes the molecule-sized liquid-vapor interface, with the large and steep but continuous change of density as well as adjacent Knudsen transition layers, which appear in nonequilibrium vapors close to interfaces and walls [29,30,32]. Sufficiently away from the interfacial region—at a distance of the order of a few mean free paths—the bulk phases obey the NSF equations.

In experiments such as those from Ward's group [15–20], the mass flow rate is sufficiently small for the reduced Eqs. (1) to be valid. Molecular scale simulations of small systems with interfaces, however, are often performed under conditions of strong nonequilibrium [5,7] for

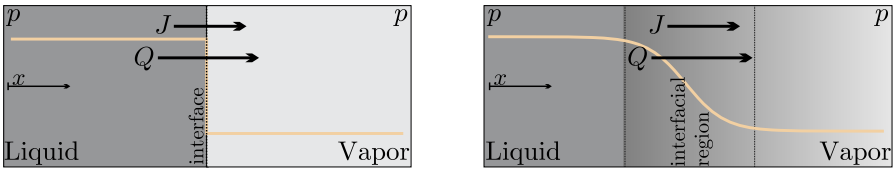


a) sharp interface b) diffuse interface

**Fig. 1.** Geometry for 1D steady state evaporation and condensation processes, distinguishing different resolutions for sharp (low resolution) and diffuse (high resolution) interfaces. The underlaid curves give an indication of the corresponding mass density profiles in equilibrium. $J$ and $Q$ are the overall mass and energy flows, and $p$ is the common pressure in the bulk phases.

which Eqs. (1) might not be valid. Differences in the bulk pressures of the phases offer a first indicator, for more insight one should check whether the higher order contributions to the conservation laws are sufficiently small.

## 3. Sharp interface model

We briefly review the standard model for sharp interfaces in nonequilibrium processes [10,12,49]. To connect bulk transport equations for adjacent liquid and vapor regions jump relations are needed. Since the interface does neither produce nor destroy mass, momentum, and energy, the fluxes $(J, P, Q)$ leaving one phase are equal to those entering the other phase, that is, denoting states of liquid and vapor just at the interface with indices $L, V$, we have [10,12]

$$\begin{aligned} J_L &= J_V = J \\ p_L &= p_V = p \\ J h_L - q_L &= J h_V - q_V = Q \end{aligned} \tag{2}$$

where $q_L = -\kappa_L \frac{dT}{dx}_{|L}$ and $q_V = -\kappa_V \frac{dT}{dx}_{|V}$ are the normal heat fluxes in the two phases at the interface.

In nonequilibrium, entropy is not conserved, but must be produced, hence with direction pointing from liquid to vapor as in Fig. 1(a) the entropy balance for the interface becomes

$$J s_V + \frac{q_V}{T} = J s_L + \frac{q_L}{T} + \sigma_S \tag{3}$$

where $\sigma_S \geq 0$ is the interfacial entropy generation rate.

Eliminating $q_L$ and introducing Gibbs free energy $g(T,p) = h - Ts$, the entropy generation rate can be written as (with Einstein summation convention)

$$\sigma_S = \mathcal{F}_\alpha \mathcal{J}_\alpha \tag{4}$$

where the entropy generation is interpreted as a sum of products of thermodynamic forces $\mathcal{F}_\alpha$ and thermodynamic fluxes $\mathcal{J}_\alpha$, identified as

$$\mathcal{F} = \left\{ \frac{g_L}{T_L} - \frac{g_V}{T_V} + h_V \left( \frac{1}{T_V} - \frac{1}{T_L} \right), \frac{1}{T_V} - \frac{1}{T_L} \right\} \quad , \quad \mathcal{J} = \{ J, q_V \} \tag{5}$$

In equilibrium the forces (5) vanish, and both phases have the same temperature $T_V = T_L = T$, and identical Gibbs free energies $g_V = g_L$. This is the well known equilibrium condition for coexistence of liquid and vapor [10,50], which states that for given temperature $T$ phase equilibrium is possible only at the saturation pressure $p_{\rm sat}(T)$ with

$$p_L = p_V = p_{\rm sat}(T) \quad \text{and} \quad g_V\left(T, p_{\rm sat}(T)\right) = g_L\left(T, p_{\rm sat}(T)\right) . \tag{6}$$

We proceed based on the methods of Linear Irreversible Thermodynamics (LIT) [51,52,10,53]. If a system is in a nonequilibrium state, i.e., the thermodynamic forces are non-zero, thermodynamic fluxes occur to drive the system toward equilibrium. That is, the fluxes are driven by the forces, and must vanish in equilibrium, together with the forces. If the degree of nonequilibrium is not too strong one expects linear relations between fluxes and forces, of the form $\mathcal{F}_\alpha = r_{\alpha\beta}\mathcal{J}_\beta$ where $r_{\alpha\beta}$ is a matrix of interface resistivities, which is non-negative definite to ensure non-negative entropy generation $\sigma_S$. The matrix should be symmetric to fulfill the Onsager relations [51,10].

We prefer to work with a dimensionless resistivity matrix $\hat{r}_{\alpha\beta}$, which is introduced such that the force-flux relations read [54]

$$\begin{bmatrix} \frac{p_{\rm sat}(T_L)}{\sqrt{2\pi R T_L}} \left[ \frac{g_L}{RT_L} - \frac{g_V}{RT_V} + h_V \left( \frac{1}{RT_V} - \frac{1}{RT_L} \right) \right] \\ \frac{p_{\rm sat}(T_L)}{\sqrt{2\pi R T_L}} T_L \left[ \frac{1}{T_V} - \frac{1}{T_L} \right] \end{bmatrix} = \begin{bmatrix} \hat{r}_{11} & \hat{r}_{12} \\ \hat{r}_{21} & \hat{r}_{22} \end{bmatrix} \begin{bmatrix} J \\ \frac{q_V}{RT_L} \end{bmatrix} . \tag{7}$$

In this formulation forces and fluxes are rescaled, with all having the units of $J$.

Often one is interested in processes where deviations from equilibrium are small. We express the forces to leading order in the deviations from equilibrium

$$\Delta p = p - p_{\rm sat}(T_L) \quad , \quad \Delta T = T_V - T_L . \tag{8}$$

By means of Taylor expansion and thermodynamic property relations $\left(\frac{\partial g}{\partial p}\right)_T = \frac{1}{\rho}$, $\left(\frac{\partial g}{\partial T}\right)_p = -s$ [50], the force-flux relations reduce to

$$\begin{bmatrix} \frac{p_{\rm sat}(T_L)}{RT_L} \left[ \frac{1}{\rho_V^{\rm sat}} - \frac{1}{\rho_L^{\rm sat}} \right] \frac{\Delta p}{\sqrt{2\pi R T_L}} \\ - \frac{p_{\rm sat}(T_L)}{\sqrt{2\pi R T_L}} \frac{\Delta T}{T_L} \end{bmatrix} = \begin{bmatrix} \hat{r}_{11} & \hat{r}_{12} \\ \hat{r}_{21} & \hat{r}_{22} \end{bmatrix} \begin{bmatrix} J \\ \frac{q_V}{RT_L} \end{bmatrix} . \tag{9}$$

Evaporation is also widely considered in kinetic theory of ideal gases using sharp interface models. Macroscopic interfacial boundary models derived from kinetic theory interface models lead to the classical phenomenological Hertz-Knudsen and Schrage formulas, as well as to their extensive refinements, based on the solution of the Boltzmann equation for the vapor phase [55–65,12,54] or more complex fluid models [66,67].

From a kinetic theory model that relies on a constant (i.e., molecular energy independent) condensation coefficient $\psi$ and full thermalization of re-emitted molecules, Cipolla et al. [58] found the simple resistivity matrix

$$\hat{r}^{KT1}_{\alpha\beta} = \begin{bmatrix} \frac{1}{\psi} - 0.40044 & 0.126 \\ 0.126 & 0.2905 \end{bmatrix} . \tag{10}$$

Application of this model to Ward's measurements on water close to the triple point [15]—where the vapor certainly behaves as an ideal gas—does not yield the observed large temperature jumps [68], implying that this model underestimates the resistivities. It is easily seen that better agreement between the measurements quoted above and kinetic theory predictions is obtained by considering small values of $\psi$ and allowing for a small accommodation coefficient of reflected molecules.

## 4. Enskog-Vlasov moment model

### 4.1. Motivation

Modeling kinetic effects at the liquid-vapor interface by the Boltzmann equation [29–32] is subject to limitations. Indeed, the Boltzmann equation is restricted to ideal gases, where the fluid's natural spatial scale, i.e., the mean free path, is much larger than the molecular size. As a consequence, the Boltzmann equation cannot describe the liquid phase but only an adjacent ideal vapor phase and necessarily phenomenological boundary conditions at the interface have to be prescribed [69–72,58,12,11].

The Enskog-Vlasov (EV) equation is a modification of the Boltzmann equation in the spirit of the Enskog kinetic theory [25] for the dense hard sphere fluid. At the expense of *ad hoc* assumptions about pair spatial and velocity correlations [28], the EV equation is based on the one-particle distribution function, just as the Boltzmann equation. Within the assumptions described below, it provides a unified description of the liquid and vapor phases, connected by a fully resolved interface [23,24]. The EV equation is not limited to ideal vapor phases, with the thermal equation of state in uniform equilibrium regions being of the generalized van der Waals class [27]. Moreover, no interface conditions have to be prescribed at the liquid-vapor interface because the latter is part of the flow region described by the EV equation.

On the other hand, within the framework of the classical kinetic theory of dilute gases, a number of mathematical methods have been developed to replace the complicated structure of the Boltzmann equation with simpler fluid equations, yet capable of providing an accurate description of kinetic regimes. A notable example of those is represented by the method of moments from which one can derive macroscopic transport equations from the Boltzmann equation, that go beyond classical hydrodynamic theory, the so-called moment equations, where classical hydrodynamics is included as the limit for small mean free path [44,45,31,73,32].

Solutions of moment equations are in good agreement with solutions of the Boltzmann equation, and can give deeper insight into processes, in particular Knudsen layers and other rarefaction effects [74]. Evaporation/condensation boundary conditions from kinetic theory can be incorporated [75,76]. Compared to solutions of the full Boltzmann equation, the numerical effort required for the solution of moment systems is significantly smaller.

Application of the moment method is not limited to the Boltzmann equation but extends to any kinetic description of fluids based on the one-particle distribution function [28]. Hence, as with the Boltzmann equation, one might either solve the EV equation itself, e.g., by means of the DSMC method [37,36,35,77], or develop, study, and solve extended moment equations. As for the ideal gas case, these moment equations and their solutions promise fast access to accurate solutions of processes, and deeper insight into processes at phase interfaces.

Recently we derived a set of 26 moment equations from the Enskog-Vlasov equation [42]. For the limit of ideal gases, the EV26 equations reduce to the well-known 26 moment equations (linearized) of kinetic theory [32]. In the hydrodynamic limit, they agree with established results [28]. The EV26 equations retain non-linear terms that are required to study the influence of the interface on the variables, when linearized, they agree with previous work for dense gases [78]. The detailed derivation of the equations was presented in [42], below we will only give a rather short summary of the equations, already reduced to 1D geometry in steady state processes.

In principle, the EV 26 equations are well suited to study phase interfaces, and to determine interfacial resistivities. As partial differential equations, they give deterministic results, and require far less numerical effort than DSMC or MD simulations. The 26 moment system shows qualitative agreement with DSMC results of the EV equation, but it will be seen that their quantitative agreement is somewhat limited, to states not too far from the critical point.

### 4.2. Enskog-Vlasov equation

In the form presented below, the Enskog-Vlasov equation describes a monatomic fluid whose atoms have mass $m$ and interact pairwise by forces derived by the Sutherland radial potential [79]

$$\phi(r) = \begin{cases} \infty & r < a \\ \phi_t(r) & r \geq a \end{cases} , \tag{11}$$

resulting from the superposition of a purely repulsive hard sphere potential and an attractive soft tail $\phi_t(r)$. In Eq. (11), $a$ is the hard sphere diameter and $r$ the distance between the centers of two interacting atoms.

The EV equation is obtained from the exact BBGKY hierarchy [28,80] by assuming that the pair distribution function can be factorized as the product of two one-particle distributions, evaluated at different positions and velocities, and a pair correlation function. Then, the hard sphere and soft tail potentials receive a different treatment as to pair correlations. The former gives rise to Enskog's dense hard sphere collision integral [25]

$$S_{\mathrm{En}} = a^2 \int_0^{2\pi} \int_0^{\pi/2} \left\{ \begin{array}{l} Y\left(\rho\left(x_r + \frac{ak_r}{2}\right)\right) f\left(x_s + ak_s, c_s^{1\prime}\right) f\left(x_t, c_t^{\prime}\right) \\ -Y\left(\rho\left(x_r - \frac{ak_r}{2}\right)\right) f\left(x_s - ak_s, c_s^{1}\right) f\left(x_t, c_t\right) \end{array} \right\} \times g \cos\theta \sin\theta d\theta d\varepsilon d\mathbf{c}^1 , \tag{12}$$

which takes into account only spatial correlations through the pair correlation function $Y(\rho)$ at contact position. In Eq. (12), $k_k = \{\cos\varepsilon \sin\theta, \sin\varepsilon \sin\theta, \cos\theta\}_k$ is the collision (unit) vector, $\rho = m \int f d\mathbf{c}$ is the mass density. In the following, the pair correlation function $Y$ is assigned, following the Standard Enskog Theory (SET) [81], as a function of the density, corresponding to its value in the hard sphere gas in uniform equilibrium. In this framework, $Y(\rho)$ bears a very simple relationship with the hard sphere fluid pressure equation of state. The latter is well approximated by a simple algebraic expression proposed by Carnahan and Starling [86] which leads to

$$Y(\rho) = \frac{1}{2}\frac{2-\eta}{(1-\eta)^3} , \quad \eta = \frac{\pi}{6}\frac{a^3}{m}\rho . \tag{13}$$

The Enskog term accounts for the spatial variation of the distribution function on the scale of the molecule diameter $a$: the colliding molecules have centers at $x_s$ and $x_s \pm ak_s$, with different values of the distribution at those points. The pair correlation function $Y$ strongly enhances the repulsive effect of hard sphere collisions where the reduced density $\eta$ is not negligible, thus forbidding molecules to occupy the same position.

Pair correlations are ignored in dealing with the contribution of the soft tail potential $\phi_t$ which takes the form of a self-consistent force field $F_k$, determined by a linear, non-local functional of the fluid density,

$$F_k(\mathbf{x}, t) = \int_{\|\mathbf{x}^1 - \mathbf{x}\| > a} \frac{d\phi_t}{dr} \frac{x_k^1 - x_k}{|\mathbf{x}^1 - \mathbf{x}|} n\left(x_r^1, t\right) d\mathbf{x}^1 \tag{14}$$

In other words, instead of considering attractive forces between individual molecules, the Vlasov force only considers the overall effect of these forces on a molecule. Specifically, the Vlasov force $F_k$ is the mean force exerted on a molecule at $\mathbf{x}$ from molecules at all other locations $\mathbf{x}^1$, based on the number density $n\left(\mathbf{x}^1\right) = \frac{\rho(\mathbf{x}^1)}{m}$ [26].

Taking into account Eqs. (12), (14), the EV equation reads

$$\frac{\partial f}{\partial t} + c_k \frac{\partial f}{\partial x_k} + F_k\left(x_l\right) \frac{\partial f}{\partial c_k} = S_{\mathrm{En}}(f, f) \tag{15}$$

where $\mathbf{x}$, $t$, and $\mathbf{c}$ denote space, time, and microscopic velocity, $f(\mathbf{x}, t, \mathbf{c})$ is the velocity distribution function, and external body forces such as gravity are ignored. In the following developments, the attractive tail potential has been assumed to have the form

$$\phi_t(r) = -\phi_a \left(\frac{r}{a}\right)^{-\gamma} \tag{16}$$

where $\phi_a > 0$ is the depth of the potential well at $r = a$ and the exponent $\gamma > 0$ has been set equal to 6 to mimic the attractive tail of the Lennard-Jones potential.

It is also interesting to note that, in general, it is possible to express the Vlasov force (14) as the divergence of a tensor $\mathcal{T}^K$ [80]:

$$F_k = -\frac{1}{\rho}\frac{\partial \mathcal{T}^K_{ks}}{\partial x_s} \tag{17}$$

Expanding the density in the integrand of Eq. (14), the familiar form of the Korteweg tensor is obtained,

$$\mathcal{T}^K_{ks} = -\frac{2\pi}{3}\frac{a^3}{m}\frac{\gamma\phi_a}{\gamma-3}\rho^2\delta_{ks} - \frac{2\pi}{15}\frac{a^5}{m}\frac{\gamma\phi_a}{\gamma-5}\left[\left(\rho\frac{\partial^2\rho}{\partial x_r\partial x_r} + \frac{1}{2}\frac{\partial\rho}{\partial x_r}\frac{\partial\rho}{\partial x_r}\right)\delta_{ks} - \frac{\partial\rho}{\partial x_s}\frac{\partial\rho}{\partial x_k}\right] . \tag{18}$$

In the expression above, the first term describes the pressure reduction due to attractive forces, just as it appears in the van der Waals equation [50]. The second term describes capillary forces due to density gradients, including surface tension in the liquid-vapor interface, where the density gradient is steep [43]; this expression also appears in the square gradient theory [87–89].

To complete the theoretical framework of the present form of EV equation, it is to be noted that proofs of the H-theorem (i.e., agreement with the 2nd law of thermodynamics) are available for the modified or revised Enskog theory (RET) [82] and for the Boltzmann-Enskog equation (BE) [83,84], but not (so far) for the standard Enskog theory (SET) used here.

In RET, the uniform equilibrium pair correlation function $Y$ of SET is replaced by a complex non-local functional of the density field which would make both numerical and analytical treatments much more difficult. On the other hand, BE keeps the non-local structure of the SET collision term but assumes $Y \equiv 1$, thus oversimplifying the fluid physics. Lack of proof does not imply lack of proper physics since numerical simulations of the hard sphere fluid based on SET are in excellent agreement with "exact" MD simulations [34].

Moment equations are approximations of the underlying kinetic equation and typically only approximate the second law behavior of the kinetic equation. While it is not possible to find a general entropy and entropy balance for the moment system, one always finds a quadratic entropy for linearized systems, and observes proper dissipative behavior for nonlinear moment equations in a wide range of process parameters [85]. All moment solutions exhibit proper physical behavior.

Finally, it should be stressed that the EV equation (15) provides a simplified description of a fluid whose atoms interact through the potential described above. It can be viewed as a kinetic extension of Diffuse Interface Models (DIM) [43] which have the capability of giving a unified description of two-phase flows but, unlike the EV equation, cannot describe kinetic layers next to liquid-vapor interfaces [4]. As such, the EV equation cannot compete with MD as to the level of detail of atomic motion description. Yet, its description of two-phase flows is sufficiently accurate in comparison with MD simulation [36]. Moreover, its fluid description, being based on the one-particle distribution function, allows for illuminating analytical treatments [24] which complement methods based on computer algorithms and are further developed in the next sections.

### 4.3. Grad's method of moments

The aim of the Grad moment method is to replace the detailed kinetic equation through a set of moment equations that describe the main characteristics of the kinetic equation [45,31,32]. In general notation, one chooses a set of $N$ moments

$$u_A = \int \varphi_A(c_i)\, f\, d\mathbf{c}, \quad A = 1, \ldots, N \tag{19}$$

where the $\varphi_A(c_i)$ are a set of suitable polynomials. Multiplication of the kinetic equation (15) with $\varphi_A$ and integration over the microscopic velocity generates the corresponding set of moment equations

$$\frac{\partial u_A}{\partial t} + \frac{\partial V_{Ak}}{\partial x_k} = F_k U_{Ak} + P_A \ , \ A = 1, \ldots, N \tag{20}$$

where

$$V_{Ak} = \int \varphi_A(c_i)\, c_k f\, d\mathbf{c} \ , \ P_A = \int \varphi_A(c_i)\, S(f)\, d\mathbf{c} \ , \quad U_{Ak} = \int \frac{\partial \varphi_A(c_i)}{\partial c_k} f\, d\mathbf{c}. \tag{21}$$

To obtain a closed set of equations, constitutive relations are required to link the fluxes $V_{Ak}$, the productions $P_A$, and the self-productions $U_{Ak}$ to the moments $u_A$, which are chosen as the variables of the system of equations.

For moment equations of the Boltzmann equation, Grad solved the closure problem by constructing a distribution function that depends explicitly on the moments [45], written as a disturbance of the equilibrium solution,

$$f_G \simeq f_{|E}\left[1 - \lambda_A(u_B)\,\varphi_A(c_i)\right] \tag{22}$$

Here, $f_{|E} = \frac{\rho}{m}\sqrt{\frac{m}{2\pi kT}}^3 \exp\left[-\frac{mC^2}{2k_BT}\right]$ denotes the local Maxwellian equilibrium distribution, and the $\lambda_A$ are expansion coefficients (also, Boltzmann constant $k_B$, thermodynamic temperature $T$, peculiar velocity $C_i = c_i - v_i$, macroscopic velocity $v_i$). Insertion of the Grad distribution (22) into the moment definition (19) identifies the coefficients $\lambda_A$ as functions of the moments $u_A$, and then its use in the expressions (21) gives explicit local constitutive relations of the form $V_{Ak}(u_B)$, $U_{Ak}(u_B)$, $P_A(u_B)$. Inserting these into (20) finally gives the Grad moment system for the chosen set of moments. For further discussion on, e.g., the number of moments, alternative closures etc., we refer the reader to the scientific literature [45,31,32,74].

### 4.4. Enskog-Vlasov 26 moment equations

The Grad closure can be used for moment equations of the EV equation as well. However, in the context of the EV model, the above program of the Grad closure is considerably harder since the non-local terms in the Enskog collision term stand in the way. In order to obtain explicit equations, we had to use Taylor expansion of the non-local terms with the molecule diameter $a$ as smallness parameter. Moreover, we restricted the theory to reasonably small deviations from equilibrium states, which include density gradients in the equilibrium phase interface. Accordingly, the final equations are linear in gradient terms of all properties except the density. A full account of the derivation including all assumptions, and showing the complete equations in 3D, is given in [42]. Below, we only present the steady state case in 1D as pertinent for heat and mass transfer across the interface.

#### 4.4.1. Variables

Based on our experience of approximating the Boltzmann equation with moment systems [32,74] we consider a set of 26 variables, where the number refers to the 3D case. For continuity with previous work on ideal gases, we chose the variables

$$\rho = m\int f\, d\mathbf{c} = mn$$
$$\rho v_i = m\int c_i f\, d\mathbf{c}$$
$$\rho\epsilon = \frac{m}{2}\int C^2 f\, d\mathbf{c} = \frac{3}{2}\rho RT = \frac{3}{2}\rho\theta$$
$$\sigma_{ij} = m\int C_{\langle i}C_{j\rangle} f\, d\mathbf{c} \tag{23}$$

$$\mathfrak{q}_i = \frac{m}{2}\int C^2 C_i f\, d\mathbf{c}$$
$$m_{ijk} = m\int C_{\langle i}C_j C_{k\rangle} f\, d\mathbf{c}$$
$$\Delta = m\int C^4\left(f - f_{|E}\right) d\mathbf{c}$$
$$R_{ij} = m\int C^2 C_{\langle i}C_{j\rangle} f\, d\mathbf{c} - 7\theta\sigma_{ij}$$

Here, $C_i = c_i - v_i$ is the peculiar velocity, i.e., the molecule velocity observed from the co-moving frame, and indices in angular brackets indicate symmetric and trace-free tensors. The first 5 moments, $\rho$, $\rho v_i$ and $\rho\epsilon$ are mass density, momentum density, and density of thermal energy, where $\theta = RT$ is the temperature in units of specific energy, $R = k_B/m$ is the gas constant, $k_B$ is the Boltzmann constant, and $T$ is kinetic temperature. The other variables are nonequilibrium moments, which vanish in equilibrium states. Kinetic stress tensor $\sigma_{ij}$ and kinetic heat flux $\mathfrak{q}_i$ are the kinetic contributions to overall stress and energy flux; in the equations below there will be additional contributions from the Enskog and Vlasov terms. The variables $m_{ijk}$, $\Delta$, and $R_{ij}$ were constructed to be of second order in the case of Maxwell molecules [32].

For one-dimensional flows as in Fig. 1, we only need one component of each tensor, which gives the eight variables

$$u_A = \left(\rho,\ v,\ \theta,\ \sigma,\ \mathfrak{q},\ m_{111},\ \Delta,\ R_{11}\right)\ , \tag{24}$$

where $\sigma = \sigma_{11}$, $\mathfrak{q} = \mathfrak{q}_1$. Their respective transport equations are found from the full equations in [42] by reducing these for steady state and 1D, as listed below. Due to the expansions required to find the moments of the Enskog collision term, the equations contain a large number of terms of various orders. Due to the use of dimensionless equations, the order of the various terms is not as easily recognized, for full insight the interested reader is referred to [42].

#### 4.4.2. Dimensions

The only parameters that determine the EV model are molecule diameter $a$, molecule mass $m$, strength of potential $\phi_a$, and potential exponent $\gamma$. We present the equations, and their solutions, in dimensionless units, which are chosen such that

$$a = m = \phi_a = 1 \tag{25}$$

With this, length $x$ is measured in multiples of $a$, density $\rho$ in multiples of $\frac{m}{a^3}$, temperature $\theta = RT$ in multiples of $\phi_a$, and time $t$ in multiples of $a/\sqrt{\phi_a}$. Moreover, data and figures shown below are for power potentials with $\gamma = 6$, such that

$$\chi_1 = \frac{\gamma}{\gamma-3} = 2\ ,\quad \chi_3 = \frac{\gamma}{\gamma-5} = 6\ . \tag{26}$$

#### 4.4.3. Mass balance

The mass balance states that for 1D steady state processes the mass flux $J$ is constant,

$$\frac{d\rho v}{dx} = 0 \implies J = \rho v = const. \tag{27}$$

#### 4.4.4. Momentum balance

The momentum balance states that the total momentum flux $P$ is a constant with several contributions that are described below,

$$\frac{dP}{dx} = 0 \quad\implies\quad P = \rho v^2 + p + P_\sigma + P_{\text{Vlasov}} + P_{\text{Enskog}} = const. \tag{28}$$

The first term, $\rho v^2$, describes convective momentum transfer. The equilibrium pressure

$$p = \rho\theta\left(1 + \frac{2\pi}{3}\rho Y\right) - \frac{2\pi}{3}\chi_1\rho^2 \tag{29}$$

is a non-monotonous function of density, with the same principal features as the van der Waals equation of state, and hence allows for phase separation. Evaluation in equilibrium by means of Maxwell's equal area rule [50] yields critical point temperature, pressure and mass density as $\theta_{\text{crit}} = 0.7546$, $p_{\text{crit}} = 0.06748$, $\rho_{\text{crit}} = 0.249$ [42].

Viscous stresses are found as

$$P_\sigma = \left(1 + \frac{2}{5}\frac{2\pi}{3}\rho Y\right)\sigma - \frac{4}{5}\sqrt{\pi}\frac{\rho^2 Y}{\sqrt{\theta}}\left(\theta\frac{dv}{dx} + \frac{1}{10}\frac{d\frac{\mathfrak{q}}{\rho}}{dx} + \frac{1}{42}\frac{d\frac{m_{111}}{\rho}}{dx}\right) \tag{30}$$

where the contributions with kinetic stress $\sigma$ and the velocity gradient are present also on the NSF level, while the terms with $\mathfrak{q}$ and $m_{111}$ describe thermal stresses and other higher order effects.

Phase separation with diffuse interface becomes possible, since the non-monotonous pressure is balanced by capillary stresses, which create the required surface tension. The main contribution comes from the Vlasov force with the Korteweg stress (18),

$$P_{\text{Vlasov}} = -\frac{2\pi}{15}\chi_3\left(\rho\frac{d^2\rho}{dx^2} - \frac{1}{2}\frac{d\rho}{dx}\frac{d\rho}{dx}\right) \tag{31}$$

The Enskog collision term gives a smaller contribution of the form

$$P_{\text{Enskog}} = \frac{\pi}{60}\left(\frac{d^2Y\rho^2\theta}{dx^2} + 3Y\frac{d^2\rho^2\theta}{dx^2} - 12Y\frac{d\rho}{dx}\frac{d\rho\theta}{dx} \underline{- \frac{1}{2}\theta\rho^2\frac{d^2Y}{d\rho^2}\frac{d\rho}{dx}\frac{d\rho}{dx}}\right), \tag{32}$$

where the underlined term is an ad-hoc addition that ensures validity of the equal area rule in the numerical solutions of the EV26 equation [90, 42]; without the correction there is a small deviation of the saturation pressure of less than 1% relative to that from the equal area rule.

#### 4.4.5. Balance of thermal energy

Within the Enskog-Vlasov model, one has to account for thermal, kinetic and Vlasov energies, where balances of kinetic and Vlasov energies are found from the balances of momentum and mass, respectively [91–93,42]. The balance of thermal energy reads in compact form

$$\frac{d}{dx}\left[\frac{3}{2}\rho\theta v + q\right] = -\rho\theta\left(1 + \frac{2\pi}{3}\rho Y\right)\frac{dv}{dx} - \left(P_\sigma + P_{\text{Enskog}}\right)\frac{dv}{dx} \tag{33}$$

where $\frac{3}{2}\rho\theta v$ is the convective flux of thermal energy, $q$ is the non-convective heat flux, the first expression on the right hand side is the work for volume change, and the second expression is frictional heating, which was ignored in [42] due to linearization.

The non-convective heat flux has several contributions,

$$q = \left(1 + \frac{3}{5}\frac{2\pi}{3}\rho Y\right)\mathfrak{q} - \frac{2}{3}\sqrt{\pi}\sqrt{\theta}\rho^2 Y\frac{d\theta}{dx} - \sqrt{\pi}\frac{\rho^2 Y}{\sqrt{\theta}}\left[\frac{4}{15}\theta\frac{d}{dx}\left(\frac{\sigma}{\rho}\right) + \frac{1}{90}\frac{d}{dx}\left(\frac{\Delta}{\rho}\right) + \frac{2}{105}\frac{d}{dx}\left(\frac{R_{11}}{\rho}\right)\right], \tag{34}$$

where the first two terms are present also on the NSF level, while the terms with $\sigma$, $\Delta$, and $R_{11}$ describe higher order effects.

#### 4.4.6. Kinetic stress and heat flux balances

Due to the many contributions from the Enskog term, the balance laws for kinetic stress and kinetic heat flux assume rather rich forms, with an abundance of higher order contributions that we do not discuss in detail. For 1D steady state processes, the equations for $\sigma$ and $\mathfrak{q}$ read

$$\left[\rho\theta\left(1 + \frac{2}{5}\frac{2\pi}{3}\rho Y\right)\right]\frac{4}{3}\frac{dv}{dx} + \frac{8}{15}\frac{d}{dx}\left[\left(1 + \frac{3}{5}\frac{2\pi}{3}\rho Y\right)\mathfrak{q}\right] + \frac{d}{dx}\left[\left(1 + \frac{6}{35}\frac{2\pi}{3}\rho Y\right)m_{111}\right] + \frac{2\pi}{3}\left[\frac{4}{25}\mathfrak{q} + \frac{8}{35}m_{111}\right]\frac{1}{\rho}\frac{d\rho^2 Y}{dx} - \sqrt{\pi}\sqrt{\theta}\left[\frac{16}{45}\rho^2\frac{d}{dx}\left(Y\frac{d\theta}{dx}\right) + \frac{32}{45}\rho Y\frac{d\rho}{dx}\frac{d\theta}{dx}\right] - \frac{\sqrt{\pi}}{\sqrt{\theta}}\left[\frac{4}{675}\rho\frac{d}{dx}\left(Y\frac{d\Delta}{dx}\right) - \frac{4}{675}\Delta\frac{d}{dx}\left(Y\frac{d\rho}{dx}\right)\right]$$

$$
\begin{aligned}
&- \sqrt{\pi}\sqrt{\theta}\left[\frac{88}{315}\rho\frac{d}{dx}\left(Y\frac{d\sigma}{dx}\right) - \frac{304}{315}\sigma\frac{d}{dx}\left(Y\frac{d\rho}{dx}\right) - \frac{6}{35}\rho\sigma\frac{d^2Y}{dx^2}\right]\\
&- \frac{\sqrt{\pi}}{\sqrt{\theta}}\left[\frac{44}{2205}\rho\frac{d}{dx}\left(Y\frac{dR_{11}}{dx}\right) - \frac{2}{45}R_{11}\frac{d}{dx}\left(Y\frac{d\rho}{dx}\right) - \frac{3}{490}\rho R_{11}\frac{d^2Y}{dx^2}\right]\\
&= -\frac{16}{5}\rho\sqrt{\pi\theta}Y\left(\sigma + \frac{1}{28}\frac{R_{11}}{\theta}\right) . \qquad (35)
\end{aligned}
$$

$$
\begin{aligned}
&\frac{5}{2}\rho\theta\left(1+\frac{3}{5}\frac{2\pi}{3}\rho Y\right)\frac{d\theta}{dx} + \theta\frac{d}{dx}\left[\left(1+\frac{3}{5}\frac{2\pi}{3}\rho Y\right)\sigma\right]\\
&- \frac{\sigma}{\rho}\theta\frac{d}{dx}\left[\left(1+\frac{9}{10}\frac{2\pi}{3}\rho Y\right)\rho\right] + \frac{1}{2}\frac{d}{dx}\left[\left(1+\frac{12}{35}\frac{2\pi}{3}\rho Y\right)R_{11}\right]\\
&+ \frac{1}{6}\frac{d}{dx}\left[\left(1+\frac{3}{5}\frac{2\pi}{3}\rho Y\right)\Delta\right] + \frac{2\pi}{3}\left[\frac{1}{30}\frac{\Delta}{\rho} + \frac{11}{140}\frac{R_{11}}{\rho}\right]\frac{d\rho^2Y}{dx}\\
&+ \frac{19}{5}\sqrt{\pi}\sqrt{\theta}\theta\frac{d}{dx}\left(\rho^2Y\frac{dv}{dx}\right) - \sqrt{\pi}\sqrt{\theta}\left[\frac{27}{50}\rho\frac{d}{dx}\left(Y\frac{d\mathfrak{q}}{dx}\right)\right.\\
&\left.- \frac{37}{30}\mathfrak{q}\frac{d}{dx}\left(Y\frac{d\rho}{dx}\right) - \frac{8}{75}\rho\mathfrak{q}\frac{d^2Y}{dx^2}\right] - \sqrt{\pi}\sqrt{\theta}\left[\frac{9}{70}\rho\frac{d}{dx}\left(Y\frac{dm_{111}}{dx}\right)\right.\\
&\left.- \frac{1}{6}m_{111}\frac{d}{dx}\left(Y\frac{d\rho}{dx}\right) - \frac{1}{105}\rho m_{111}\frac{d^2Y}{dx^2}\right]\\
&= -\frac{2}{3}\frac{16}{5}\rho\sqrt{\pi\theta}Y\mathfrak{q} . \qquad (36)
\end{aligned}
$$

#### 4.4.7. Higher order moments $m_{ijk}$, $\Delta$, $R_{ij}$

Finally, the equations for the higher moments couple these to the previous and among themselves,

$$
\begin{aligned}
&\frac{9}{5}\theta\frac{d}{dx}\left[\left(1+\frac{6}{35}\frac{2\pi}{3}\rho Y\right)\sigma\right] - \frac{9}{5}\frac{\theta\sigma}{\rho}\frac{d}{dx}\left[\left(1+\frac{2}{5}\frac{2\pi}{3}\rho Y\right)\rho\right]\\
&+ \frac{9}{35}\frac{d}{dx}\left[\left(1+\frac{12}{35}\frac{2\pi}{3}\rho Y\right)R_{11}\right] + \frac{279}{2450}\frac{2\pi}{3}\frac{R_{11}}{\rho}\frac{d\rho^2Y}{dx}\\
&- \sqrt{\pi}\sqrt{\theta}\frac{8}{175}\theta\frac{d}{dx}\left(\rho^2Y\frac{dv}{dx}\right) + \sqrt{\pi}\sqrt{\theta}\left[\frac{4}{25}\mathfrak{q}\frac{d}{dx}\left(Y\frac{d\rho}{dx}\right)\right.\\
&\left.- \frac{108}{875}\rho\frac{d}{dx}\left(Y\frac{d\mathfrak{q}}{dx}\right) + \frac{8}{875}\rho\mathfrak{q}\frac{d^2Y}{dx^2}\right]\\
&+ \sqrt{\pi}\sqrt{\theta}\left[\frac{39}{35}m_{111}\frac{d}{dx}\left(Y\frac{d\rho}{dx}\right) - \frac{23}{175}\rho\frac{d}{dx}\left(Y\frac{dm_{111}}{dx}\right)\right.\\
&\left.+ \frac{43}{175}\rho m_{111}\frac{d^2Y}{dx^2}\right] = -\frac{3}{2}\frac{16}{5}\rho\sqrt{\pi\theta}Ym_{111} . \qquad (37)
\end{aligned}
$$

$$
\begin{aligned}
&8\theta\frac{d}{dx}\left[\left(1+\frac{3}{5}\frac{2\pi}{3}\rho Y\right)\mathfrak{q}\right] - 8\theta\frac{\mathfrak{q}}{\rho}\frac{d}{dx}\left[\left(1+\frac{4}{5}\frac{2\pi}{3}\rho Y\right)\rho\right]\\
&- \sqrt{\pi}\sqrt{\theta}\left[\frac{4}{3}\rho^2\theta\frac{d}{dx}\left(Y\frac{d\theta}{dx}\right) + \frac{8}{3}\theta\rho Y\frac{d\rho}{dx}\frac{d\theta}{dx}\right]\\
&- \sqrt{\pi}\sqrt{\theta}\left[\frac{8}{15}\rho^2\theta\frac{d}{dx}\left(Y\frac{d\frac{\sigma}{\rho}}{dx}\right) - \frac{32}{3}\rho\theta Y\frac{d\rho}{dx}\frac{d\frac{\sigma}{\rho}}{dx}\right]\\
&- \sqrt{\pi}\sqrt{\theta}\left[\frac{1}{3}\rho\frac{d}{dx}\left(Y\frac{d\Delta}{dx}\right) - \frac{31}{45}\Delta\frac{d}{dx}\left(Y\frac{d\rho}{dx}\right) - \frac{4}{45}\Delta\rho\frac{d^2Y}{dx^2}\right]\\
&- \sqrt{\pi}\sqrt{\theta}\left[\frac{4}{7}\rho\frac{d}{dx}\left(Y\frac{dR_{11}}{dx}\right) - \frac{76}{105}R_{11}\frac{d}{dx}\left(Y\frac{d\rho}{dx}\right)\right.\\
&\left.- \frac{4}{105}\rho R_{11}\frac{d^2Y}{dx^2}\right] = -\frac{2}{3}\frac{16}{5}\rho\sqrt{\pi\theta}Y\Delta . \qquad (38)
\end{aligned}
$$

$$
\begin{aligned}
&\frac{56}{15}\theta\frac{d}{dx}\left[\left(1+\frac{12}{35}\frac{2\pi}{3}\rho Y\right)\mathfrak{q}\right] - \frac{56}{15}\theta\frac{\mathfrak{q}}{\rho}\frac{d}{dx}\left[\left(1+\frac{1}{2}\frac{2\pi}{3}\rho Y\right)\rho\right]\\
&+ 2\theta\frac{d}{dx}\left[\left(1+\frac{12}{35}\frac{2\pi}{3}\rho Y\right)m_{111}\right]\\
&- 2\frac{m_{111}\theta}{\rho}\frac{d}{dx}\left[\left(1+\frac{11}{14}\frac{2\pi}{3}\rho Y\right)\rho\right]\\
&- \sqrt{\pi}\sqrt{\theta}\left[\frac{16}{45}\rho^2\theta\frac{d}{dx}\left(Y\frac{d\theta}{dx}\right) + \frac{32}{45}\rho\theta Y\frac{d\rho}{dx}\frac{d\theta}{dx}\right]\\
&- \sqrt{\pi}\sqrt{\theta}\left[\frac{4}{45}\rho\frac{d}{dx}\left(Y\frac{d\Delta}{dx}\right) - \frac{76}{675}\Delta\frac{d}{dx}\left(Y\frac{d\rho}{dx}\right) - \frac{4}{675}\rho\Delta\frac{d^2Y}{dx^2}\right]\\
&- \sqrt{\pi}\sqrt{\theta}\left[\frac{88}{315}\rho\theta\frac{d}{dx}\left(Y\frac{d\sigma}{dx}\right) - \frac{28}{45}\theta\sigma\frac{d}{dx}\left(Y\frac{d\rho}{dx}\right) - \frac{3}{35}\rho\theta\sigma\frac{d^2Y}{dx^2}\right]\\
&- \sqrt{\pi}\sqrt{\theta}\left[\frac{44}{147}\rho\frac{d}{dx}\left(Y\frac{dR_{11}}{dx_r}\right) - \frac{2369}{2205}R_{11}\frac{d}{dx}\left(Y\frac{d\rho}{dx}\right)\right.\\
&\left.- \frac{1709}{8820}\rho R_{11}\frac{d^2Y}{dx^2}\right] = -\frac{16}{5}\rho\sqrt{\pi\theta}Y\left[\frac{1}{2}\theta\sigma + \frac{205}{168}R_{11}\right] . \qquad (39)
\end{aligned}
$$

### 4.5. Hydrodynamics (NSF)

The above EV26 equations account for higher orders on the scale of the molecule diameter, as is necessary for the resolution of the interface. In the bulk phases sufficiently away from the interface, the capillary forces vanish, $P_{\text{Vlasov}} = P_{\text{Enskog}} = 0$, and the flow is described by the bulk Navier-Stokes-Fourier (NSF) equations, which are obtained from Chapman-Enskog expansion. First order expansion of the equations for non-conserved moments yields (in 1D)

$$
\begin{aligned}
\sigma^{(\text{NSF})} &= -\frac{205}{202}\sqrt{\theta}\frac{\left(1+\frac{2}{5}\frac{2\pi}{3}\rho Y\right)}{\frac{16}{5}\sqrt{\pi}Y}\frac{4}{3}\frac{dv}{dx} ,\\
\mathfrak{q}^{(\text{NSF})} &= -\frac{15}{4}\sqrt{\theta}\frac{\left(1+\frac{3}{5}\frac{2\pi}{3}\rho Y\right)}{\frac{16}{5}\sqrt{\pi}Y}\frac{d\theta}{dx} , \qquad (40)\\
R_{11}^{(\text{NSF})} &= -\frac{84}{205}\theta\sigma^{(\text{NSF})} ,\\
\Delta^{(\text{NSF})} &= m_{111}^{(\text{NSF})} = 0 .
\end{aligned}
$$

By inserting these into the conservation laws we identify viscous stresses and thermal energy flux as the 1D Navier-Stokes-Fourier expressions

$$
P_\sigma^{(\text{NSF})} = -\left[\frac{205}{202}\sqrt{\theta}\frac{\left(1+\frac{2}{5}\frac{2\pi}{3}\rho Y\right)^2}{\frac{16}{5}\sqrt{\pi}Y}\frac{4}{3} + \frac{4}{5}\sqrt{\pi}\rho^2Y\sqrt{\theta}\right]\frac{dv}{dx} , \qquad (41)
$$

$$
q^{(\text{NSF})} = -\left[\frac{15}{4}\sqrt{\theta}\frac{\left(1+\frac{3}{5}\frac{2\pi}{3}\rho Y\right)^2}{\frac{16}{5}\sqrt{\pi}Y} + \frac{2}{3}\sqrt{\pi}\sqrt{\theta}\rho^2Y\right]\frac{d\theta}{dx} . \qquad (42)
$$

The factors in the brackets are the overall viscosity and heat conductivity for the Enskog gas. These expressions agree with [28], where, however, the factor $\frac{205}{202}$ is replaced by unity; this small difference is due to the influence of the higher order moment equation for $R_{11}$ which was not considered in the reference.

Inserting stress and heat flux into the conservation laws yields, after some algebra, the steady state form of the NSF equations in the bulk phases,

$$
\begin{aligned}
\rho v &= J = const. ,\\
\rho v^2 + p + P_\sigma^{(\text{NSF})} &= P = const , \qquad (43)\\
\left(h + \frac{v^2}{2}\right)J + q^{(\text{NSF})} + P_\sigma^{(\text{NSF})}v &= Q = const. .
\end{aligned}
$$

Here the bulk enthalpy for the model was identified as

$$
h = \left(\frac{5}{2} + \frac{2\pi}{3}\rho Y\right)\theta - \frac{4\pi}{3}\chi_1\rho . \qquad (44)
$$

From this, internal energy $u$ appears as the sum of thermal and Vlasov energies

$$
u = h - \frac{p}{\rho} = \frac{3}{2}\theta - \frac{2\pi}{3}\chi_1\rho , \qquad (45)
$$

and bulk entropy is found by means of the Gibbs equation $T ds = du - \frac{p}{\rho^2} d\rho$ as

$$s = \frac{3}{2} \ln\theta - \ln\rho - \frac{3 - \frac{\pi}{3}\rho}{\left(1 - \frac{\pi}{6}\rho\right)^2} \,. \tag{46}$$

These property relations are required to find resistivities from (7).

The simulations yield kinetic heat flux $\mathbf{q}$, which in the NSF realm is related to actual heat flux $q$ through a factor that depends only on density,

$$q^{(\mathrm{NSF})} = \left[1 + \frac{3}{5}\frac{2\pi}{3}\rho Y + \frac{128\pi}{225}\frac{\rho^2 Y^2}{1 + \frac{3}{5}\frac{2\pi}{3}\rho Y}\right] \mathbf{q}^{(\mathrm{NSF})} \tag{47}$$

EV-NSF solutions for two phase systems rely on the conservation laws for mass, momentum and energy (27), (28), (33) with the above constitutive relations and the Vlasov and Enskog stresses (31), (32), corresponding to the Diffuse Interface Model derived by the EV equation.

### 4.6. EV13 equations for 13 moments

In order to obtain better insight into the capabilities of EV-moment equations, we also consider a simpler system with 13 moments, just as in the well-known Grad13 equations [44,45,32]. These are obtained from the larger EV26 set by setting the higher moments $m_{ijk}, \Delta, R_{ij}$ to zero, and ignoring their equations. In 1D, the model has the five variables $\rho, v, \theta, \sigma, \mathbf{q}$, which follow from (27), (28), (33), (35), (36) with $m_{111} = \Delta = R_{11} = 0$.

### 4.7. EV26R: ad-hoc regularization for $m_{ijk}$, $\Delta$, $R_{ij}$

As will be seen, the numerical results for EV26 indicate overly strong heat and mass transfer resistance of the interface for conditions further away from the critical point. By comparison with DSMC results and analysis of the transport equations, we could identify overly large values for the higher moments $m_{111}$, $\Delta$, $R_{11}$ as the cause for the extra resistance.

Within the philosophy of the moment method, lack of agreement with solutions of the underlying kinetic equation points to an insufficient number of moments used. While the non-trivial derivation of an extended moment system is planned for the future, below we consider an ad-hoc correction based on the R26 moment system, which is the regularization of the Grad 26 moment system in classical kinetic theory [46]. For this, we added the leading regularization terms for the moments $m_{111}$, $\Delta$, $R_{11}$ as determined by Gu & Emerson [46] to the left hand side of the respective moment equations, which read (the ellipses stand for the full lhs of Eqs. (37), (38), (39))

$$\begin{aligned}
&\cdots - 1.09\frac{d}{dx}\left[\mu\frac{d}{dx}\left(\frac{m_{111}}{\rho}\right)\right] = -\frac{3}{2}\frac{16}{5}\rho\sqrt{\pi\theta}Y m_{111} \\
&\cdots - \frac{7}{3}\frac{d}{dx}\left[\mu\frac{d}{dx}\left(\frac{\Delta}{\rho}\right)\right] - 4\left[\mu\frac{d}{dx}\left(\frac{R_{11}}{\rho}\right)\right] = -\frac{2}{3}\frac{16}{5}\rho\sqrt{\pi\theta}Y\Delta \\
&\cdots - 1.363\frac{d}{dx}\left[\mu\frac{d}{dx}\left(\frac{R_{11}}{\rho}\right)\right] = -\frac{16}{5}\rho\sqrt{\pi\theta}Y\left[\frac{1}{2}\theta\sigma + \frac{205}{168}R_{11}\right]
\end{aligned} \tag{48}$$

Here, $\mu$ is the viscosity coefficient of the gas, for which we use the Enskog-Vlasov expression

$$\mu = \sqrt{\theta}\frac{\left(1 + \frac{2}{5}\frac{2\pi}{3}\rho Y\right)^2}{\frac{16}{5}\sqrt{\pi}Y} \,. \tag{49}$$

These additional terms have a significant influence on the results, in particular they lead to improved results for heat transfer processes, as will be seen below. We emphasize that this is an ad-hoc correction which in the future must be replaced by a proper account of the influence of higher moments as predicted by the moment equations of the EV equation for increased number of variables, e.g., by an extension of the order of magnitude method outlined in Ref. [94].

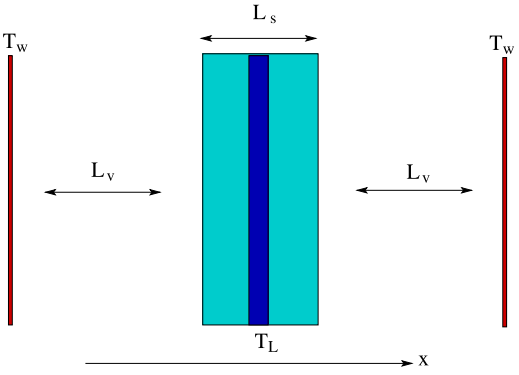


**Fig. 2.** Test problem geometry.

## 5. Numerical solutions of the EV and EV moment equations

### 5.1. DSMC solutions of the EV equation

The accuracy of the moment approximations described above has been assessed by solving Eq. (15) numerically by the extension to dense gases [35,36] of the well known Direct Simulation Monte Carlo (DSMC) particle scheme, first proposed by G. A. Bird in 1963 [37], for dilute gases governed by the Boltzmann equation [29].

Two distinct but complementary problems have been considered. The first one consists in describing energy transport in the two-phase system depicted in Fig. 2.

An infinite liquid slab of nominal thickness $L_s$ occupies the central region of the gap separating two identical parallel solid walls. The two symmetrically disposed regions between each liquid interface and its nearest wall have nominal width $L_v$ and are occupied by the vapor phase. A central strip of the liquid slab is thermostatted at temperature $T_L$ by a Berendsen thermostat [95], whereas the solid walls are both assigned the identical temperature $T_w \geq T_L$.

The temperature $T_L$ is assumed to be lower than the Enskog-Vlasov fluid critical temperature and, for any given system geometry, $T_w$ is limited by the condition that a stable liquid slab is formed in the steady state.

In the assumption that fluid properties gradients, generated by the temperature difference $T_w - T_L$, are normal to the walls and liquid slab interfaces, the steady, spatially one-dimensional version of Eq. (15) is solved. The spatial coordinate $x$ spans the gap between the walls, respectively located at $x_w^{\pm} = \pm\left(L_v + \frac{L_s}{2}\right)$. At the wall location, the boundary conditions for the distribution function $f(x, \mathbf{c}, t)$ are assigned as

$$\begin{aligned}
f(x_w^-, \mathbf{c}, t) &= \frac{n_w^-(t)}{\left(2\pi RT_w\right)^{3/2}} \exp\left(-\frac{\mathbf{c}^2}{2RT_w}\right), \quad c_1 > 0 \\
f(x_w^+, \mathbf{c}, t) &= \frac{n_w^+(t)}{\left(2\pi RT_w\right)^{3/2}} \exp\left(-\frac{\mathbf{c}^2}{2RT_w}\right), \quad c_1 < 0
\end{aligned} \tag{50}$$

being $n_w^{\pm}(t)$ wall densities to be computed from the flux of impinging molecules on each wall, as:

$$n_w^{\pm}\sqrt{\frac{RT_w}{2\pi}} = \int\limits_{\mathbf{c}\cdot\hat{\mathbf{x}}^{\pm}>0} \left(\mathbf{c}\cdot\hat{\mathbf{x}}^{\pm}\right) f(x_w^{\pm}, \mathbf{c}, t)\, d\mathbf{c}, \quad \hat{\mathbf{x}}^{\pm} = \mp\hat{\mathbf{x}} \tag{51}$$

being $\hat{\mathbf{x}}$ the unit vector associated with the coordinate $x$.

The boundary conditions (50) specify that molecules hitting a solid wall are instantaneously reflected in the domain and thermalized to $T_w$. Condition (51) states that mass fluxes are zero at walls at any time and

guarantee that the mass flux $J$ in the whole domain is uniformly equal to zero in steady flow conditions.

The zero mass flux condition and the conservation of momentum along the $x$ direction lead to the uniformity of the normal stress in the domain.

In absence of net mass flux, the temperature jump $\Delta T$ at the liquid-vapor interface and the pressure difference $\Delta p$ (see Eq. (8)) are only determined by the heat flux, according to Eq. (9). Hence the analysis of the obtained numerical solution for this test problem allows obtaining resistivities $\hat{r}_{12}$ and $\hat{r}_{22}$.

The second test problem consists in the classical steady evaporation of an infinite, planar liquid surface into a half-space [64,65,11], in which the downstream subsonic vapor flow is in isothermal equilibrium uniquely determined by the mass flux $J$. In this case, the heat flux contribution in Eq. (9) is zero hence $\Delta T$ and $\Delta p$ are determined by $J$. Accordingly, numerical solutions of the EV equation for this test problem provide estimates of resistivities $\hat{r}_{11}$ and $\hat{r}_{21}$.

DSMC simulations for the second problem can be performed in the same geometry described by Fig. 2. A net mass flux is obtained by making walls permeable. An identical absorption probability $P_{abs}$ is assigned to the walls, respectively located at $x_w^{\pm}$. Whenever a particle hits a wall it is either absorbed with probability $P_{abs}$ or re-emitted into the vapor phase according to the distribution function (50), with probability $\left(1 - P_{abs}\right)$. In order to keep the interface steady, absorbed particles are re-inserted at random in the thermostatted region of the liquid slab at each time step, their new velocities being sampled from a Maxwellian with zero bulk velocity and temperature $T_L$. Wall temperature, $T_w$, is tuned to obtain a uniform temperature profile in the equilibrium vapor regions sufficiently far from the Knudsen layers adjacent to the interface and walls, respectively.

It should be observed that steady, one-dimensional solutions of the EV equation, with the geometry and boundary conditions specified above, are symmetric with respect to the plane $x = 0$. Doubling the domain size (and particle number) of DSMC simulations, although unnecessary at first glance, avoids adopting complicated numerical boundary conditions at the symmetry plane. Moreover, doubling the domain size and the flow symmetry can be exploited to double the particle sample size while estimating macroscopic fields.

The results of each DSMC simulation, shown in Sections 6 and 7 for the heat transfer and evaporation problems, respectively, have been obtained by a combination of time and phase averaging. The latter has been obtained by superposing the time averaged results of 20 statistically independent simulations of the (macroscopically) same system. Each individual simulation has been started by a condition in which the liquid slab is in equilibrium with the vapor at temperature $T_L$. Particle motion is then computed till the onset of steady flow conditions. After the transient is over, the sampling of particle microscopic quantities is performed, along with the motion calculation, to obtain macroscopic quantities. The number of particles per simulation ranged from $6 \times 10^5$ to $8 \times 10^5$, hence the total number of particles involved in the phase averaging ranged from $1.2 \times 10^7$ to $1.6 \times 10^7$.

The typical overall computing time amounted to about 40 hours, on a 20-core Xeon™ machine, to complete a cycle of $1.2 \times 10^6$ time steps, which included both the transient and the sampling time intervals. The considerable amount of computational resources provided an acceptable estimation of the higher order moments appearing in the EV26 formulation which exhibit both small amplitudes and high variance. In each simulation, the nominal extent of the vapor regions, $L_v$, has been chosen wide enough to obtain a well defined hydrodynamic vapor region, separating the two kinetic layers next to the vapor liquid interface and its facing wall.

A few observations about DSMC solutions accuracy are in order, before describing and discussing simulations results. The first one is about computed mass flux profiles, shown in Fig. 3a, in the case of evaporation simulations. Fig. 3a compares two $J$ profiles computed for the same physical setup, using two different values of the time step $\Delta t$. Both profiles differ from a constant in two regions. The first one coincides with the thermostatted liquid strip, where the mass flux is not constant because of the addition of particles that were absorbed at the outer boundaries.

The second one consists of a narrow peak confined in the liquid-vapor interface region. The peak, whose amplitude is proportional to $\Delta t$, is an artifact of the DSMC first-order time scheme which advances the particle positions and velocities by a pure advection step, followed by a collision step. In the particular problems considered here, the mean field $F_x$ compresses the slab during the advection step, whereas the slab expands during the collision step. Since particle velocities are sampled at the end of the collision step, the peak reflects the intense, nonlocal, collisional momentum transfer in the interface region, with its high density gradient. As Fig. 3a shows, the peak superposes to a constant mass flux profile which is left unchanged by the time step reduction which only affects the peak amplitude.

The second important quantity appearing in the estimation of resistivities is the normal stress $P$, defined by Eq. (28). The latter is computed as the sum of its kinetic, collisional (hard sphere) and attractive tail contributions. The last two contributions, respectively denoted as $P_{Enskog}$ and $P_{Vlasov}$ in Eq. (28), result from nonlocal interactions and have complicated expressions, in general [80]. In the case of the present problem geometry, they can be computed as

$$P_{Vlasov}(x) = -\int_{x_w^-}^{x} n(y) F_1(y)\, dy \tag{52}$$

$$P_{Enskog}(x) = -\int_{x_w^-}^{x} \dot{Q}_1(y)\, dy \tag{53}$$

$$\dot{Q}_1 = m \int c_1 S_{En}\, d\mathbf{c} \tag{54}$$

being $n$ the number density and $\dot{Q}_1$ the collisional rate of change of momentum along $x_1$. The latter quantity is easily evaluated by accumulating molecular velocities changes, due to binary hard sphere collisions, in each cell, during the sampling time interval. The evaluation of $P_t$ involves the mean field component $F_1$ which is assumed constant in each spatial DSMC cell, being computed by the following one-dimensional version of Eq. (14):

$$F_1(x_1|t) = 2\pi\phi_a \left[ a^\gamma \int_{|x_1 - x_1'|>a} \frac{(x_1' - x_1) n(x_1'|t)}{|x_1 - x_1'|^\gamma}\, dx_1' + \int_{|x_1 - x_1'|\le a} (x_1' - x_1) n(x_1'|t)\, dx_1' \right] \tag{55}$$

At each position $x_1$, $F_1(x_1|t)$ is obtained as a linear functional of $n$. The kernel in the integral has an infinite range and is truncated at a prescribed value of $|x_1 - x_1'|$ in the numerical implementation of Eq. (55). As in the case of MD simulations [95], potential range truncation affects fluid properties in general and the pressure equation of state in particular. Fig. 3b shows $P$ profiles obtained by liquid-vapor equilibrium simulations at $T = 0.50$ for three different values of the kernel cutoff distance. The computed $P$ profiles are fairly constant through the liquid, interface and vapor regions and not much affected by the cutoff distance. However, as expected, $P$ deviates from the exact equilibrium pressure, as given by Eq. (29) for the smaller values of the cutoff distance. Actually, the numerical equation of state does not coincide with the exact one, because of the truncation and, to a lesser extent, because of the integral discretization. The deviation is more evident in the liquid bulk because the tiny liquid density variations, caused by changing the cutoff distance, correspond to relatively large pressure variations.

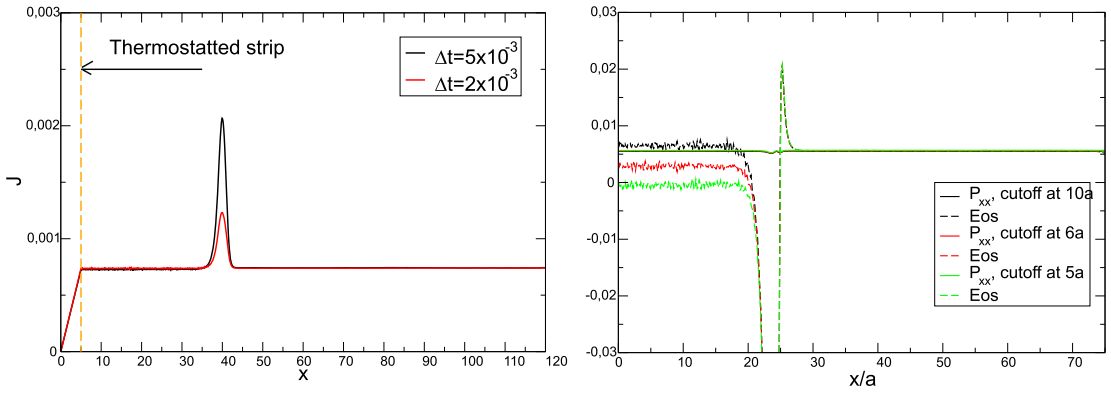


**Fig. 3.** (a) Effect of $\Delta t$ on mass flux $J$: $T_L = 0.60$, $T_w = 0.5564$, $P_{abs} = 0.1$. (b) Equilibrium density profiles: $T/T_c = 0.596$ (∘), $T/T_c = 0.663$ (□), $T/T_c = 0.729$ (⋄), $T/T_c = 0.795$ (△), $T/T_c = 0.862$ (▽). Algebraic potential tail with $\gamma = 6$.

In spite of the deviations from the exact equation of state, computations with the smallest cutoff distance, $5a$, are consistent and computationally less expensive. Moreover, the computed liquid-vapor coexistence curve is very close to the one used in the moment method calculation, based on the exact equation of state and the equal area rule. Hence, as a rule, the cutoff distance has been set equal to five hard sphere diameters. The grid size has been set to $a/10$ and the time stepto $5 \times 10^{-3} a \sqrt{\frac{m}{\phi_a}}$. Further refinements of space and time discretization did not produce changes which affect the comparison with the moment method predictions of nonequilibrium flows described below.

A second cause of deviation of DSMC computed pressure from the exact equation of state is the overestimation of the collision rate affecting high density flow regions. The observed deviation, which can be as high as 0.5% of the exact collision rate, is caused by the strong nonlinearity of the factor $Y$ that enhances the hard sphere collision rate in high density regions. In presence of the DSMC density fluctuations, positive density deviations from the average contribute to the collision rate more than negative ones. The effect on the pressure is a small but evident overestimation of the hard sphere contribution.

The pressure will still exhibit a constant profile, since the particles dynamics will find a steady state where kinetic, collisional and mean field contributions equilibrate each other. Being caused by density fluctuations, the effect can be mitigated by increasing the particle number or by smoothing the density field.

In this work, in general, a high number of simulation particles has been used for high order moment estimations. Hence, no correction of the hard sphere collision rate has been necessary.

### 5.2. Numerical solutions of EV moment equations

#### 5.2.1. Geometry and boundary conditions

Unlike in the DSMC setup that uses a specularly duplicated spatial domain, moment equations have been solved for 1D steady problems involving a single interface, subjected to mass and/or heat transfer, such as sketched in Fig. 1. Specifically we study systems of overall length $L$, with the interface centered at location $L_0$, separating the liquid on the left from the vapor on the right. Domain length $L$ and location $L_0$ of the interface are chosen such that all interface details, e.g., the diffuse liquid-vapor interface and the adjacent Knudsen layer, are located within the domain, with enough space to fully develop hydrodynamic regions on both sides of the liquid-vapor interface. The solid boundaries, present in DSMC simulations, are not necessary and they have not been considered.

Then, towards the boundaries of the system, at $x = 0$ and $x = L$, the bulk phases obey the NSF equations (40) which are taken as boundary conditions for the higher moments at both sides. Further, we control the constant mass flux $J$ and the boundary temperature $\theta_{bL}$ of the liquid at $x = 0$. On the vapor side, at $x = L$, we either prescribe the vapor temperature $\theta_{bV}$ or, for an adiabatic boundary, set the temperature gradient, and hence $\mathfrak{q}_V$, to zero. The given boundary conditions suffice to solve the problem. We note that one can either control the system pressure or the mass flux, but not both independently. Prescription of the mass flux is the easier choice.

#### 5.2.2. Solution method

To solve the EV26 (as well as EV-NSF, EV13, EV26R) with the above boundary conditions, all equations are discretized taking fourth order finite differences on a uniform grid with $n$ grid points at locations $x_k$ $(k = 1, \dots n)$.

Considering that we had to understand the behavior of the EV moment equations first, we chose a non-optimized method of solution, using the `fsolve(eqs,y0)` routine of matlab, which finds the solution `y` to a set of equations `eqs(y)=0`, starting at an initial guess `y0` [47,48].

A good initial guess is crucial for finding reliable results and we used a multi-step approach to determine useful guesses. As the first step, we used the equal area rule to find saturation mass densities $\rho_{L,\mathrm{sat}}(\theta_0)$, $\rho_{V,\mathrm{sat}}(\theta_0)$ and pressure $p_{\mathrm{sat}}(\theta_0)$ for a problem-relevant temperature $\theta_0$. From the mass densities, we constructed an approximation to the equilibrium density curve as

$$\rho_0(x_k) = \rho_{V,\mathrm{sat}} + \frac{1}{2}(\rho_{L,\mathrm{sat}} - \rho_{V,\mathrm{sat}})\left[1 + \tanh(x_k - L_0)\right] \tag{56}$$

which creates a discrete density profile with the diffuse interface located at $L_0$. This profile serves as the initial guess to find the true equilibrium rest state at $\theta_0$ with densities $\rho_0^{(k)}$. This equilibrium state is used as initial guess to solve the NSF equations with the prescribed boundary conditions. Next, the numerical NSF result is used as initial guess for the solution of the EV moment equations.

As soon as one has solutions of the full EV moment equations, these can be used as initial guesses at different parameter settings as well. This is in particular convenient when searching for solutions at stronger nonequilibrium, where one can increase the mass flow (say) step by step, and use the result of a previous simulation as initial guess. Final results were checked for consistency by determining flows of mass, momentum and energy, which must be verified as constants.

For the EV26 case, the variables of the problem are the discretizations of the respective moments, plus the total momentum flux $P$,

$$\rho^{(k)},\ P,\ v^{(k)},\ \theta^{(k)},\ \sigma^{(k)},\ \mathfrak{q}^{(k)},\ m_{111}^{(k)},\ \Delta^{(k)},\ R_{11}^{(k)} \quad , \quad k = 1, \dots, n$$

Their solution follows from the eight discretized equations (27), (28), (33), (35) – (37) plus the requirement of constant mass in the system, which is fixed by the initial guess,

$$\sum_{k=1}^{n} \rho^{(k)} = \sum_{k=1}^{n} \rho_0^{(k)} = \mathcal{M}_0 \,. \tag{57}$$

The mass flux $J$ appears as a parameter in the system of equations, the boundary conditions for temperature, e.g. $\theta^{(1)} = \theta_{bL}$, replace the energy balances at the boundary points, and NSF relations (40) for higher moments are inserted in the boundary points of (35) – (37).

The equations are complex, and this method of solution is rather time consuming. Nevertheless is served well to test the equations, identify and correct errors in the equations, and to produce first results as presented below. For future work a more elaborate–and faster–implementation will be developed.

#### 5.2.3. Discretization errors

The accuracy of results depends on the grid spacing, where finer grid size reduces the errors discussed below. For results shown in the next sections, the grid spacing is chosen as $\Delta x = L/n = 0.1$.

The unavoidable numerical error can be recognized in comparing numerical equilibrium solutions to exact equilibria found from the equal area rule [50,42]. Here, the numerically found saturation pressures differ by 0.002% for $\theta = 0.52$, and 0.0002% for $\theta = 0.6$. Moreover, the Gibbs free energies of the phases, which should be equal, are slightly different.

While these errors are small, they affect the determination of resistivities, which rely on the differences of reduced Gibbs free energies $\Delta\frac{g}{T}$ (7), or the deviation of pressure from saturation pressure, $\Delta p = p - p_{\rm sat}\left(T_L\right)$ (9). As can be seen from the equations, larger fluxes $\left(J, q_V\right)$ increase the thermodynamic forces, hence for these the errors in equilibrium values will not affect the results considerably. For small fluxes, however, the respective errors can be substantial.

As an example, we consider some data for $\theta_L = 0.52$, $q_V = 0$ at various mass flows. For the equilibrium case $J = 0$ the difference in Gibbs free energies–which should be zero–is obtained as $\left[\Delta\frac{g}{T}\right]_{\rm err} = 2.25 \times 10^{-5}$, which we must consider as the error in numerical determination of $\Delta\frac{g}{T}$ for the chosen grid spacing. For $J = 10^{-6}$, the nonequilibrium difference is found as $\Delta\frac{g}{T} = 2.28 \times 10^{-4}$, which therefore is burdened by a relative error of about 10%. For larger mass flows, the error becomes smaller, e.g., 1% at $J = 10^{-5}$.

For weak nonequilibrium, where fluxes and forces are small, we can use the close to equilibrium expansion (9), which needs accurate data of $\Delta p = p - p_{\rm sat}\left(T_L\right)$. When the saturation pressure from the equal area rule is used, the relative error in $\Delta p$ is of about the same size as the error in $\Delta\frac{g}{T}$ (e.g., 1.2% for $J = 10^{-5}$). This error was reduced by using saturation pressures found from the numerical solution in equilibrium instead of saturation pressures from the equal area rule.

The errors in equilibrium data depend on the grid spacing, with the above values found for $\Delta x = 0.1$. Decrease, or increase, of the grid spacing reduces, or enlarges, the unavoidable numerical errors, which affect the accuracy of results for processes close to equilibrium. For all results shown, the deviation from equilibrium is sufficient to keep the numerical error well below 1%.

## 6. Heat transfer ($J = 0$)

### 6.1. Process curves

The simplest process involving a phase interface is pure heat transfer through a two-phase system with interface, driven by a temperature gradient, while no evaporation or condensation occurs, that is $J = 0$. Since DSMC solutions are computationally expensive, we first performed these, for appropriate system length $L$, interface location $L_0$, and boundary temperatures $\theta_{bL}$, $\theta_{bV}$. Then, in order to have a meaningful comparison between DSMC solutions and moment models, for the latter we chose the same liquid boundary temperature $\theta_{bL}$ and interface location $L_0$, and adjusted the vapor boundary temperature such that the moment models agree in the kinetic heat flux $\mathfrak{q}_V$ in the vapor with the DSMC result. This approach allowed us to use different system size $L$, $L_0$ between moment and DSMC solutions.

DSMC solutions exhibit Knudsen layer effects at the outer boundaries, in particular on the vapor side, which are not of concern for our considerations, and do not affect the comparison, since the overall heat flux is constant through the Knudsen layer. These boundary layers are not shown in the figures, which only show the interesting area around the interface.

In the three case presented below, the temperature at left boundary, $\theta_{bL}$, takes the values $0.52, 0.60, 0.65$, respectively. For these temperatures, $\lambda_v$, the equilibrium value of the mean free path in the vapor phase, normalized to the hard sphere diameter $a$, amounts respectively to $13.7, 5.33, 3.143$. In the heat transfer examples, the interface temperature is slightly higher than $\theta_{bL}$, therefore $\lambda_v$ is smaller than the corresponding equilibrium value. In the evaporation flows, the interface temperature is lower than $\theta_{bL}$ and $\lambda_v$ is accordingly higher than the corresponding equilibrium value.

All moment curves are shifted such that the location of the steepest descent of the density curve agrees with the corresponding point of the DSMC results. This point is considered as effective location of the interface, denoted as $x_\rho$, and will be used as such in the determination of resistivities. In the figures below the location $x_\rho$ is highlighted through the green dot.

Fig. 4 shows results for a DSMC simulation for a relatively dense system, not too far below the critical point ($\theta_{\rm crit} = 0.754$), with $L = 200$, $L_0 = 40$, $\theta_{bL} = 0.65$, $\theta_{bV} = 0.7$, $J = 0$. Regions further away from the interface, where NSF is valid, are not shown, the figures concentrate on the interesting interface features in the smaller interval shown. Specifically, the figures compare results for DSMC (purple), EV13 (green), EV26 (orange), the regularization EV26R (red), and NSF (brown, only the temperature curve is shown).

We briefly comment on the figures in the panel:

The curves for density (upper left) agree well for all models, but the slope from the moment models is slightly smaller than from DSMC. Indeed, it is well-known that the Korteweg approximation (31) for the stress yields less steep density profiles than the full Vlasov expression [36]. Due to the large difference between liquid and vapor densities we also show the specific volume $1/\rho$ (upper middle) which emphasizes differences in the vapor region, also here all models agree well.

The temperature curves (upper right) for all models exhibit a steeper increase of temperature at the interface, which only commences on the vapor side, for $x > x_\rho$. This increase corresponds to the temperature jump in a sharp interface model, and is due to irreversible processes in the interfacial zone, as expressed through resistivities. The size of the T-jump differs between models: Compared to DSMC, the jump is too small for NSF and EV13, but too large for EV26. The ad-hoc regularization EV26R provides a surprisingly good agreement with DSMC. The benchmark DSMC result shows weak fluctuations, which do not affect the comparison.

The pressure (middle left) is constant in the bulk regions, and shows the characteristic wiggle through the interface where it is balanced by capillary stresses (i.e., surface tension). The moment models give the same pressure for bulk liquid and vapor, and all three models agree well on pressure. Since the DSMC simulation, as explained in Section 5.1, exhibits a deviation with respect of the exact liquid pressure, we do not show the pressure $p(\rho, \theta)$ from the equation of state, but instead the normal stress $P$ as defined in (28), which is effectively constant through the domain in good agreement with the bulk pressure of the moment models.

The DSMC solutions for higher moments show more pronounced fluctuations, but nevertheless give clear indication of the spatial variation of the moments. For 1D heat transfer, the kinetic stress $\sigma$ vanishes in the NSF approximation (40), hence non-zero values of $\sigma$ indicate states of local non-equilibrium. The center figure compares $\sigma$ for the various models, where $\sigma$ differs relatively little between the moment models, with values within the DSMC results.

Kinetic heat flux $\mathfrak{q}$ (middle right) agrees due to the data matching, and for all models has rather different values in the liquid and vapor

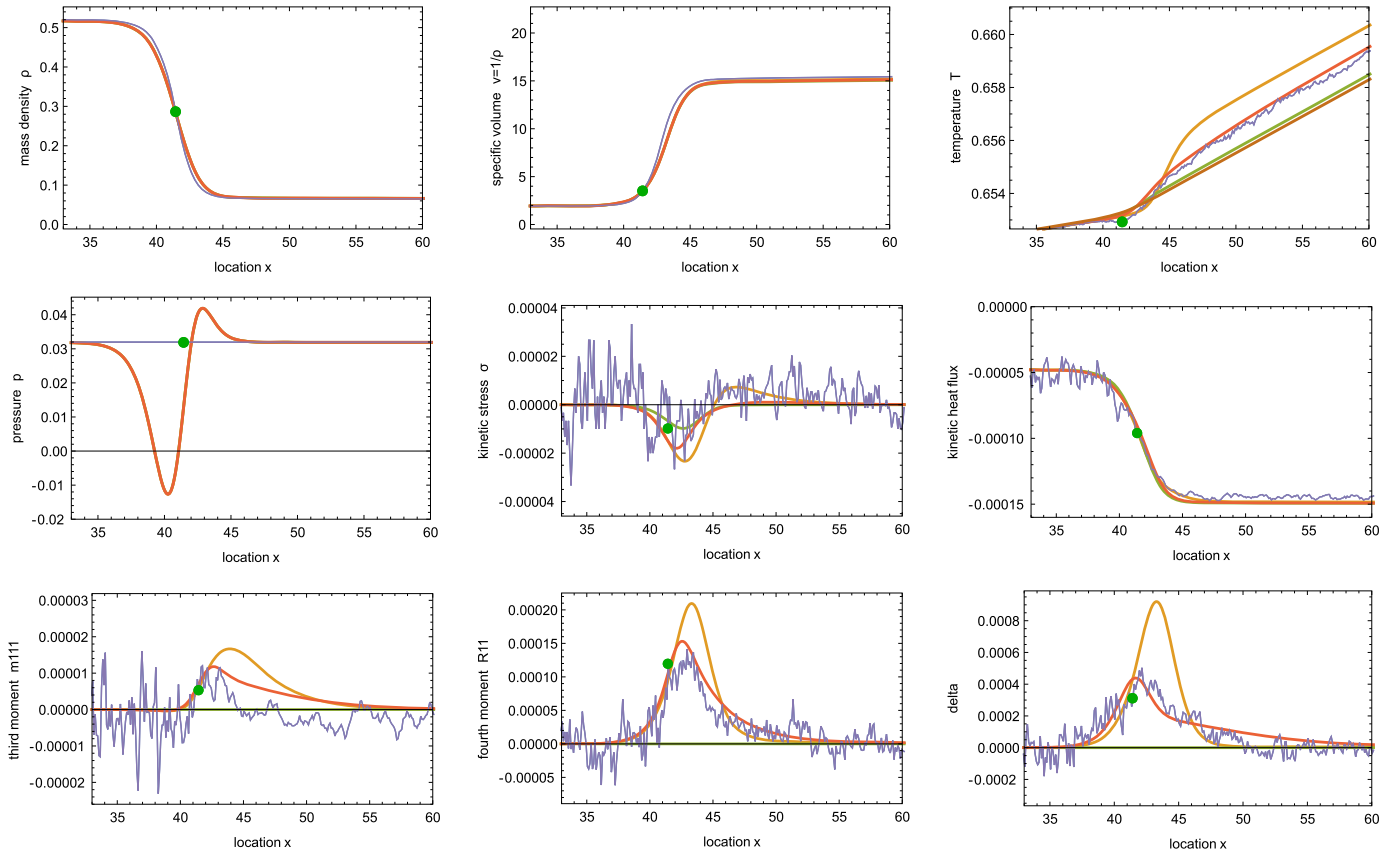


**Fig. 4.** Heat transfer without evaporation with (for DSMC) $L = 200$, $L_0 = 40$, $\theta_{bL} = 0.65$, $\theta_{bV} = 0.7$, $J = 0$. The curves show the values of the EV26 variables and pressure for the interesting interval for various moment sets: EV26 - orange, EV13 - green, EV26R - red, NSF ($T$ only) - brown, compared to EV-DSMC - purple. Green dots indicate the location $x_\rho$ of the steepest density descent. (For interpretation of the colors in the figure(s), the reader is referred to the web version of this article.)

bulk phases due to the much higher conductivity of the liquid phase. The total heat flux $q$ (not shown) is constant, its values in the bulk are obtained from the NSF relation (47) as $q = -1.64 \times 10^{-4}$ for all models.

Just as the kinetic stress $\sigma$, the higher moments $m_{111}$, $R_{11}$, and $\Delta$ (lower row) describe higher order effects that vanish in the hydrodynamic (NSF) region further away from the interface. The domain in which these variables are non-zero must be interpreted as the combined interface and Knudsen layer, which here has a thickness of $\sim 20$, quite a bit wider as the thickness of the interface as identified from the density curve ($\sim 5$). Comparison between DSMC and moment models shows that EV26 and EV26R both match the DSMC behavior, but EV26 clearly overpredicts the size of the higher moments, while the regularization EV26R leads to a rather good match.

Figs. 5 (for $L_0 = 40$, $\theta_{bL} = 0.60$, $q_V = -1.99 \times 10^{-4}$, $J = 0$) and 6 (for $L_0 = 40$, $\theta_{bL} = 0.52$, $q_V = -1.54 \times 10^{-4}$, $J = 0$) show similar figures for heat transfer at lower temperatures and similar overall heat fluxes for conditions further below the critical point.

The behavior is similar to that discussed above, with more marked differences between moment models and DSMC as the overall state of the system is at temperatures further below the critical point, where the interface is sharper, and the Knudsen layers are wider due to reduced pressure, and increased mean free path.

In particular we note the increasing deviation of temperature, where for lower temperature EV 26 (orange) significantly overpredicts the temperature jump, accompanied by overprediction of the moments $m_{111}$, $R_{11}$, $\Delta$ in the Knudsen layer zone. The regularized EV26R equations (red) fare significantly better, with good results for the case with $\theta_{bL} = 0.6$, but discrepancies, in particular too small temperature jump, for the case with $\theta_{bL} = 0.52$.

The discrepancies between DSMC and moment methods with 13 and 26 moments, and the improvement of the agreement when the regularizing terms, which approximate the influence of higher moments, are added give a clear indication that the number of moments considered here appears to be too low to obtain an authoritative moment model.

### 6.2. Deviation from local equilibrium

Since the DSMC method can not easily provide explicit information on the particle distribution function in the considered near equilibrium flow conditions, we combine moments from the DSMC calculations with the form of the distribution function used in the moment method to discuss the behavior of the distribution. The Enskog-Vlasov moment theory relies on closure based on the Grad approximation of the local distribution function (22),

$$f_G = f_{|E}\,(1 + \Phi) \tag{58}$$

where $f_{|E}$ denotes the local Maxwellian, and $\Phi$ describes the nonequilibrium contributions through the moments; for 1D geometry [42],

$$\begin{aligned}\Phi_{EV26} = {} & \frac{\sigma_{11}}{2\rho\theta^2}\left[C_1^2 - \frac{1}{2}\left(C_2^2 + C_3^2\right)\right] + \frac{2}{5}\frac{\mathfrak{q}}{\rho\theta^2}C_1\left(\frac{C_1^2 + C_2^2 + C_3^2}{2\theta} - \frac{5}{2}\right) + \\ & + \frac{m_{111}}{6\theta^3}C_1^3 + \frac{R_{11}}{14\rho\theta^3}\left[C_1^2 - \frac{1}{2}\left(C_2^2 + C_3^2\right)\right]\left(\frac{C_1^2 + C_2^2 + C_3^2}{2\theta} - \frac{7}{2}\right) \\ & + \frac{\Delta}{8\rho\theta^2}\left(1 - \frac{2}{3}\frac{C_1^2 + C_2^2 + C_3^2}{\theta} + \frac{1}{15}\frac{\left(C_1^2 + C_2^2 + C_3^2\right)^2}{\theta^2}\right).\end{aligned} \tag{59}$$

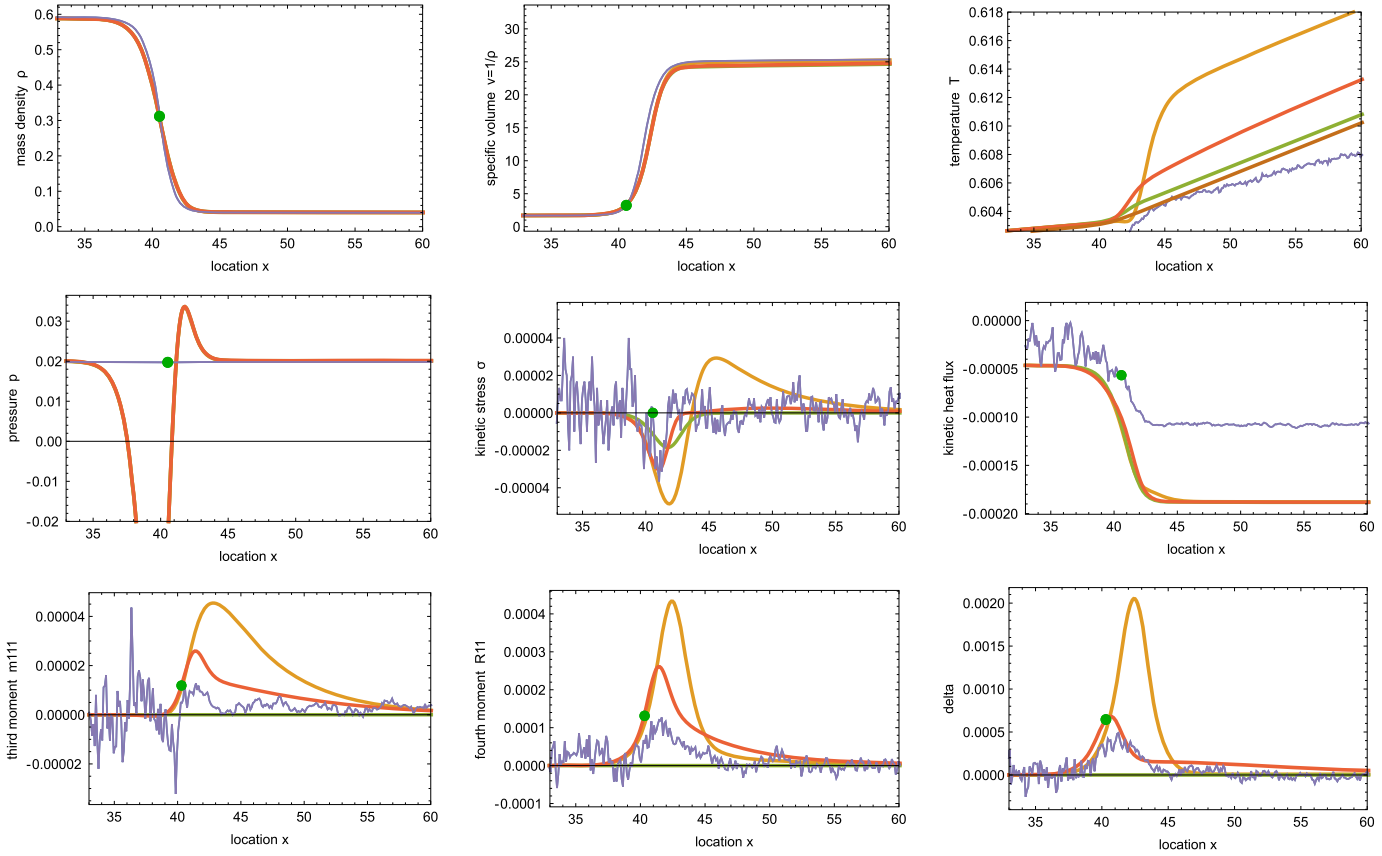


**Fig. 5.** Heat transfer without evaporation with (for DSMC) $L = 120$, $L_0 = 40$, $\theta_{bL} = 0.60$, $\theta_{bV} = 0.64$, $J = 0$. The curves show the values of the EV26 variables and pressure for the interesting interval for various moment sets: EV26 - orange, EV13 - green, EV26R - red, NSF ($T$ only) - brown, compared to EV-DSMC - purple. Green dots indicate the location $x_\rho$ of the steepest density descent.

In the hydrodynamic (NSF) regime, the nonequilibrium contribution is only due to heat transfer, with $\mathfrak{q}$ given by (40),

$$\Phi_{\rm NSF} = \frac{2}{5}\frac{\mathfrak{q}}{\rho\theta^2}C_1\left(\frac{C_1^2+C_2^2+C_3^2}{2\theta} - \frac{5}{2}\right) \tag{60}$$

While $\Phi_{\rm NSF}$ determines the difference from the NSF distribution to the local Maxwellian (where $\Phi = 0$), the difference $\Phi_{\rm EV26} - \Phi_{\rm NSF}$ is a measure for the deviation of the actual distribution from the hydrodynamic one. Since the Maxwellian suppresses contributions with large velocities, we study the dimensionless expressions

$$\Delta\hat{f}_{\rm NSF} = \hat{f}_{|\rm E} \times \left(\Phi_{\rm NSF}\right) \quad , \quad \Delta\hat{f}_{\rm NE} = \hat{f}_{|\rm E} \times \left(\Phi_{\rm EV26} - \Phi_{\rm NSF}\right) \tag{61}$$

where $\hat{f}_{|\rm E} = \exp\left[-\frac{C_1^2+C_2^2+C_3^2}{2\theta}\right]$ is a normalized Maxwellian with $\hat{f}_{|\rm E}\,(C=0) = 1$. We evaluate these functions for the case of heat transfer with $\theta_{bL} = 0.6$ (as in Fig. 5) at several locations in the domain, plotted as function of the velocities $\left(C_1, C_r = \sqrt{C_2^2+C_3^2}\right)$. We used the DSMC results for evaluation, moment solutions yield corresponding behavior. In this case, the point of steepest density decrease is at $x_\rho = 40.15$.

Fig. 7 shows the measure $\Delta\hat{f}_{\rm NSF}$ for the deviation from the local Maxwellian in the hydrodynamic case at locations in the bulk liquid (maximum value $\sim 0.0001$ at $x = 30.05$) and the bulk vapor ($\sim 0.002$ at $x = 100.05$). Through the interface the function assumes values between those of the bulk regions (not shown).

The nonequilibrium contribution $\Delta\hat{f}_{\rm NE}$ must be compared in size to $\Delta\hat{f}_{\rm NSF}$. Fig. 8 shows this function at six locations from bulk liquid through the interface to bulk vapor. Note that, just as in Fig. 7, the subfigures in Fig. 8 use different axis range in order to render meaningful functions.

Following through the plots from small to larger $x$, we observe the following, relative to the location $x_\rho$: in the bulk liquid $\Delta\hat{f}_{\rm NE}$ is significantly smaller than the NSF deviation (maximum value $\sim 0.00003$ at $x = 30.05$). Towards the interface, the value increases by more than one order of magnitude, but is still rather small at the location of steepest descent ($\sim 0.0006$ at $x = x_\rho = 40.15$). These values confirm that the liquid is well described by NSF, with the liquid region ending about the location $x_\rho$.

The most significant deviation from equilibrium is in the Knudsen layer, where the higher order moments in Fig. 5 have their peak values: the maximum value of $\sim 0.003$ at $x = 42.25$ (about two atomic diameters from $x_\rho$ towards the vapor) is larger than the hydrodynamic contribution $\Delta\hat{f}_{\rm NSF}$ anywhere in the domain. Here, the interfacial region is in a distinct non-hydrodynamic state.

Further into the vapor region, the nonequilibrium deviation decreases ($\sim 0.0008$ at $x = 50.05$) until it becomes negligibly small in the bulk vapor region ($\sim 0.00005$ at $x = 100.05$), which again is well described by NSF.

We note that for all cases the deviation from the normalized local Maxwellian $\hat{f}_{|\rm E}$ is small, with peak values well below 1%. When sampling the distribution directly from DSMC or MD simulations, the deviation from the Maxwellian will be lost in the fluctuations. Sampling of higher moments provides an accessible approach to study the deviations from equilibrium.

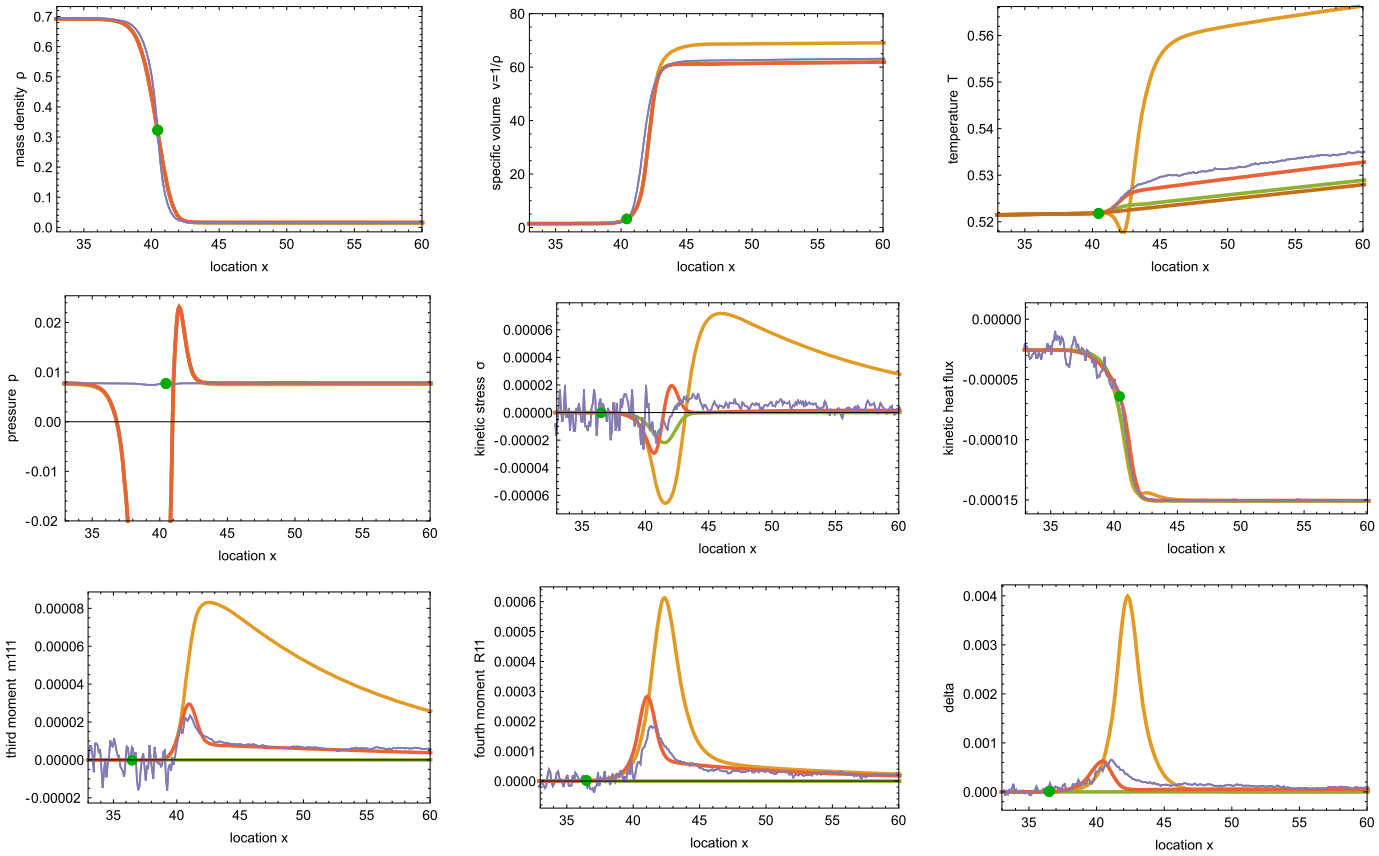


**Fig. 6.** Heat transfer without evaporation with (for DSMC) $L = 220$, $L_0 = 40$, $\theta_{bL} = 0.52$, $\theta_{bV} = 0.60$, $J = 0$. The curves show the values of the EV26 variables and pressure for the interesting interval for various moment sets: EV26 - orange, EV13 - green, EV26R - red, NSF ($T$ only) - brown, compared to EV-DSMC - purple. Green dots indicate the location $x_\rho$ of the steepest density descent.

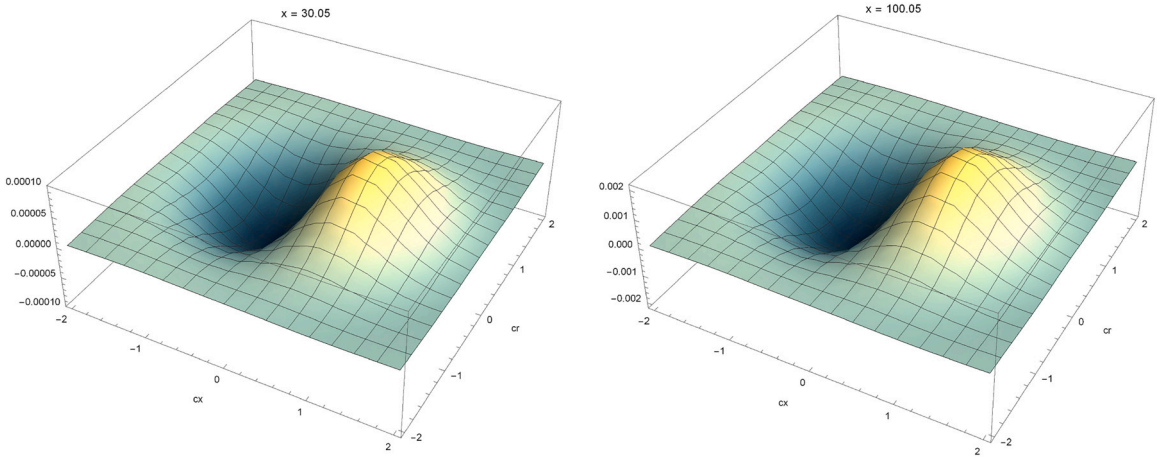


**Fig. 7.** Hydrodynamic deviation $\Delta\hat{f}_{\rm NSF} = \hat{f}_{\rm M}\Phi_{\rm NSF}$ from the local equilibrium distribution for the heat transfer process with $\theta_{bL} = 0.6$, evaluated with DSMC results in the bulk liquid and vapor regions.

### 6.3. Heat transfer resistivities

Heat transfer simulations suffice to determine two of the four resistivities $\hat{r}_{\alpha\beta}$, where (7) with $J = 0$ gives

$$\hat{r}_{12} = \frac{p_{\rm sat}(T_L)}{\sqrt{2\pi RT_L}}\left[\frac{g_L}{RT_L} - \frac{g_V}{RT_V} + h_V\left(\frac{1}{RT_V} - \frac{1}{RT_L}\right)\right]\frac{RT_L}{q_V}$$
$$\simeq -\left(\frac{1}{\rho_V} - \frac{1}{\rho_L}\right)\frac{p_{\rm sat}(T_L)}{\sqrt{2\pi RT_L}}\frac{\Delta p}{q_V} \tag{62}$$

$$\hat{r}_{22} = \frac{p_{\rm sat}(T_L)}{\sqrt{2\pi RT_L}}T_L\left[\frac{1}{T_V} - \frac{1}{T_L}\right]\frac{RT_L}{q_V} \simeq -\frac{p_{\rm sat}(T_L)}{\sqrt{2\pi RT_L}}\frac{\Delta(RT)}{q_V}\,. \tag{63}$$

These interface conditions are formulated for a sharp interface, where the properties indicated with indices $L, V$ refer to hydrodynamic data of the liquid and vapor phase directly at the interface. The connection between the microscopic simulations with diffuse interface and their smooth curves for all properties and the sharp interface model is usually done by extrapolation of bulk curves towards a suitable location within the interface, known as the dividing surface [96]. Typical choices for the location of the dividing surface are the equimolar location [53], or

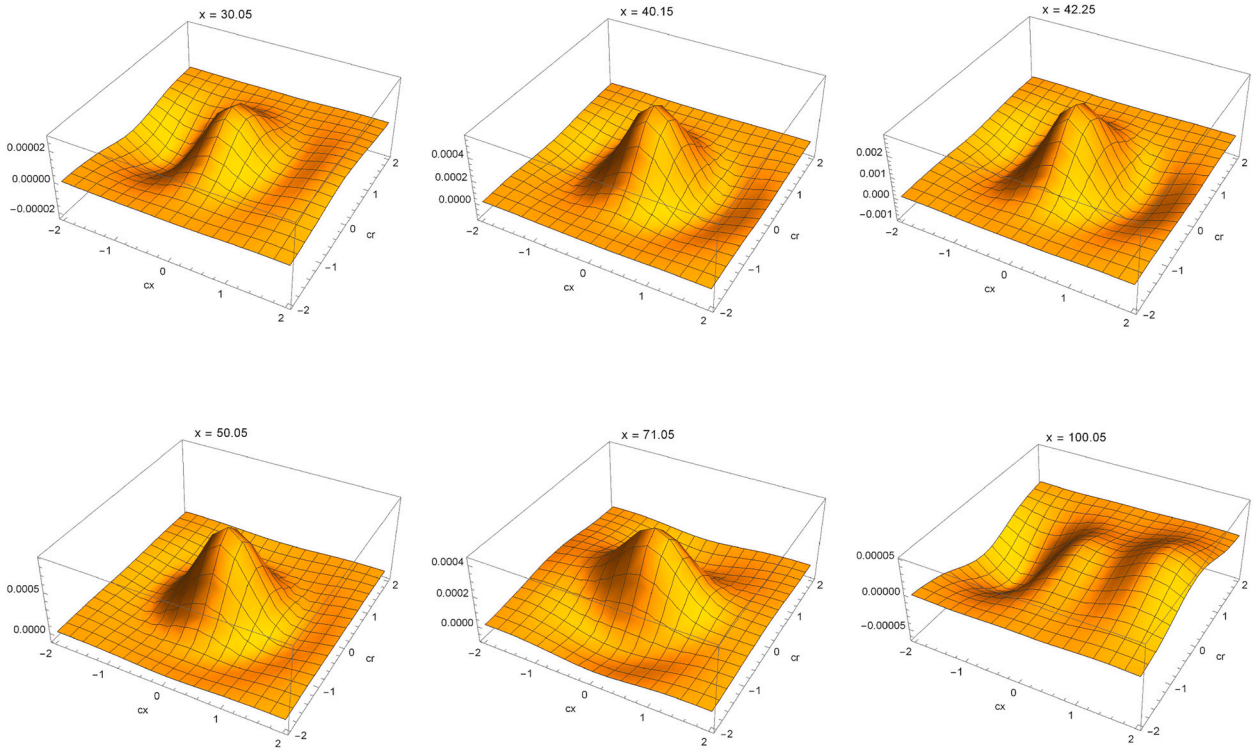


**Fig. 8.** Deviation $\Delta\hat{f}_{\rm NE} = \hat{f}_{\rm M}\left(\Phi_{\rm EV26} - \Phi_{\rm NSF}\right)$ from the hydrodynamic distribution for the heat transfer process with $\theta_{bL} = 0.6$, evaluated with DSMC results at several locations in the domain, from liquid, through interface and Knudsen layer to the hydrodynamic region.

the location of the steepest slope in density [38], $x_\rho$, which we continue to use.

As seen above, sufficiently away from the interface the microscopic solution obeys hydrodynamics (NSF), where higher moments vanish. The extrapolation is performed from the hydrodynamic region towards the location $x_\rho$ of the interface. Density $\rho$ and temperature $\theta$ are obtained directly from the simulation, and based on these, pressure $p$, enthalpy $h$, and Gibbs free energy $g = h - Ts$ are determined from the hydrodynamic relations of Sec. 4.5. For the data in our simulations, linear extrapolation suffices for density, temperature, enthalpy, and reduced Gibbs free energy $\frac{g}{RT}$.

Fig. 9 shows the extrapolation of DSMC data to $x_\rho$ relative to the property data from simulation for the case with $\theta_{bL} = 0.6$, in the vicinity of the interface, which gives $\theta_L \simeq \theta\left(x_\rho\right) = 0.603$. For other data, and for moment models, the extrapolation curves are similar.

The DSMC simulations have a small mismatch in the liquid density that leads to the observed pressure differences between bulk liquid and vapor. This mismatch is mildly reflected in values for the Gibbs free energy of the liquid, where, just as for pressure, the values are affected by mass density. With that, determination of the chemical force ($\Delta\frac{g}{T} + \cdots$) might be affected by inaccuracies that in turn lead to errors in the resistivity $\hat{r}_{12}$.

As an alternative one might use the approximation that expresses the force by the pressure deviation $\Delta p = p_V - p_{\rm sat}\left(T_L\right)$, which is obtained from first order expansion, hence valid only close to equilibrium. Just as for the moment equations, the saturation pressure obtained from DSMC simulation in equilibrium differs from that obtained from Maxwell's equal area rule due to approximation errors. Hence, for values of the resistivity $\hat{r}_{12}$ from DSMC based on $\Delta p$ we used saturation pressures $p_{\rm sat}\left(T_L\right)$ interpolated from DSMC equilibrium simulations.

Tables 1, 2 show the resulting resistivities $\hat{r}_{22}$ and $\hat{r}_{12}$ for the three cases (indicated by extrapolated liquid interface temperature $\theta_L$), as obtained from DSMC and the three sets of moment equations considered. Not surprisingly, the different methods yield significantly different values of the resistivities, that reflect the visible differences in their predictions for moments.

**Table 1**
Resistivity $\hat{r}_{22}$ from extrapolation of microscopic heat transfer solutions for DSMC (bold) and EV26R, EV26, EV13 moment equations.

| $\hat{r}_{22}$ | $\theta_L = 0.522$ | $\theta_L = 0.603$ | $\theta_L = 0.653$ |
|---|---|---|---|
| **EV-DSMC** | **0.217** | **0.177** | **0.123** |
| EV26R | 0.149 | 0.188 | 0.142 |
| EV26 | 1.027 | 0.436 | 0.223 |
| EV13 | 0.0316 | 0.0532 | 0.0391 |

We first look at values for $\hat{r}_{22}$ given in Table 1. According to (10), for the classical ideal gas case the dimensionless temperature resistivity $\hat{r}_{22}$ has a value of 0.294. The DSMC result for $\theta_L = 0.522$ differs from this value by $\sim 25\%$. As interface temperature increases, the resistivity $\hat{r}_{22}$ decreases, in agreement with the expectation that resistivities vanish at the critical point. While EV26R resistivity is of the order of that of DSMC, the temperature dependence is non-monotone. From EV26 we find significantly larger resistivities that reflect the overemphasized temperature jumps, with resistivities decreasing with increasing temperature. EV13 predicts significantly smaller resistivities with a non-monotone temperature dependence.

For the classical ideal gas with full accommodation, the resistivity $\hat{r}_{12}$ is found at a positive value of 0.126, see Eq. (10). Table 2 shows the off-diagonal resistivity $\hat{r}_{12}$, where we give results from the two forms of (62) where either difference in Gibbs free energy ($\Delta\frac{g}{RT}$) or the deviation of actual pressure from saturation ($\Delta p$) is used. The gradients are strong, hence the difference between the $\Delta\left(\frac{g}{RT}\right)$-form and the $\Delta p$-form of the equation might be due to linearization, but will also be affected by density inaccuracy in the liquid.

From the full expression with $\Delta\left(\frac{g}{RT}\right)$, DSMC predicts somewhat larger resistivity than classical kinetic theory, while for the reduced $\Delta p$ form, the resistivity is smaller, and even becomes negative for larger

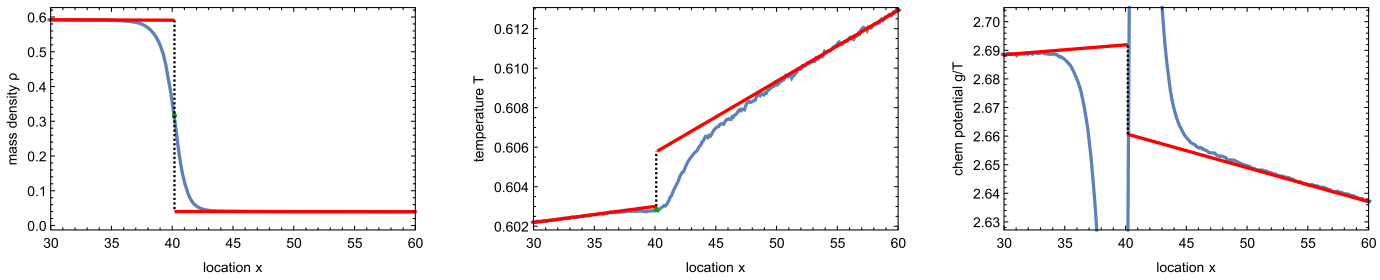


**Fig. 9.** DSMC solutions (blue) and extrapolation of hydrodynamic bulk curves to the location $x_\rho$, for density $\rho$, temperature $T$, and reduced Gibbs free energy $\frac{g}{T}$.

**Table 2**
Resistivities $\hat{r}_{12}$ from extrapolation of microscopic heat transfer solutions for DSMC (bold) and EV26R, EV26, EV13 moment equations. Left: Determined from $\Delta\frac{g}{RT}$. Right: Determined from $\Delta p$.

| $\hat{r}_{12}$ $(\Delta\frac{g}{RT})$ | $\theta_L = 0.522$ | $\theta_L = 0.603$ | $\theta_L = 0.653$ |
|---|---|---|---|
| **EV-DSMC** | **0.370** | **0.259** | **0.285** |
| EV26R | 0.144 | 0.100 | 0.122 |
| EV26 | -0.101 | 0.00647 | 0.0910 |
| EV13 | 0.0318 | 0.0575 | 0.113 |

| $\hat{r}_{12}$ $(\Delta p)$ | $\theta_L = 0.522$ | $\theta_L = 0.603$ | $\theta_L = 0.653$ |
|---|---|---|---|
| **EV-DSMC** | **0.103** | **0.0482** | **-0.0585** |
| EV26R | 0.128 | -0.0475 | -0.194 |
| EV26 | -0.219 | -0.133 | -0.220 |
| EV13 | 0.00733 | -0.112 | -0.228 |

temperature. The moment systems predict smaller absolute values of this coefficient, with different signs depending on the equation used ($\Delta\left(\frac{g}{RT}\right)$ or $\Delta p$), where the difference is due to the linearization to obtain the $\Delta p$-form, which thus does not appear to be appropriate for the strong gradients used. EV26R gives values close to the ideal gas case, while EV26 and EV13 predict relatively small values.

## 7. Forced evaporation ($q_V = 0$)

Next, we give a brief account of 1D simulations with forced evaporation, where we again compare moment results to DSMC.

### 7.1. Process curves

Mass flux through the interface and the corresponding evaporation or condensation processes have strong influence on the profiles of temperature and moments. For a clear separation of heat transfer and evaporation effects, we consider a process where the heat flux in the vapor vanishes. As in the classical evaporation into a half space [64,30], the downstream flow is characterized by a Maxwellian distribution function whose density $\rho_\infty$, temperature $T_\infty$ and velocity $v_\infty$ are determined by the mass flux $J$. In our solution procedure for moment equations, the process results from controlling boundary data, in particular setting the temperature gradient at the vapor boundary to zero, and controlling the mass flow by pumping vapor out of the system. All heat required for evaporation or condensation is transferred through the liquid phase.

Specifically, Fig. 10 shows results for a case with mass flux $J = 0.000745$, $q_V = 0$. For DSMC, the domain size is $L = 120$, $L_0 = 40$, with boundary temperatures $T_{bL} = 0.6$, $T_{bV} = 0.5564$, where the latter was adjusted to reach the adiabatic vapor state for the chosen mass flux. For the moment sets, the DSMC mass flux was prescribed, and the domain width was $L = 200$, with $L_0 = 60$ and stepsize $\Delta x = 0.1$; the temperature $T_{bL}$ of the liquid boundary was adjusted such that the temperature at the point $x_\rho$ of steepest density descent matches the DSMC data, and all curves were shifted in space to coincide in density at $x_\rho$. Again, bulk regions towards the boundaries are not shown, the figure concentrates on the interesting region around the interface; green dots highlight the location $x_\rho$ of the steepest descent of density.

We briefly comment on the figures in the panel:

Also for this process the curves for density (upper left) agree well for all models, with the slope of the moment models slightly smaller than for DSMC. The data was chosen to have agreement in the evaporation mass flux $J$ (upper middle), hence all models agree, with DSMC results showing the artificial peak at the interface as discussed above.

The figure in the upper right shows kinetic temperature $T = \theta$. The models agree on the temperature in the liquid, which results from the convective and conductive transport of the heat of vaporization through the liquid, and the boundary temperature. The results differ considerably from the location $x_\rho$ onwards into the vapor. DSMC exhibits a steep decay in temperature towards the flat profile in the vapor (the temperature jumps down), while the moment models produce distinct features as follows: EV26 temperature shows a strong and distinct valley in the Knudsen layer region that leads to a temperature that is slightly above the temperature at $x_\rho$, that is a temperature jump upwards (corresponding to negative value for $\hat{r}_{21}$). In contrast, EV13 shows a temperature overshoot in the interfacial area, with an even larger resulting temperature jump upwards. Also the regularized EV26R equations show the overshoot, but give a temperature jump downwards, which is visibly smaller than that of DSMC. The NSF solution, which assumes local equilibrium through the interface, shows a relatively weak decrease of temperature.

The pressure curve (middle left) agrees between the moment models, with bulk pressures in liquid and vapor at the same value, and in good agreement with the normal stress $P$ for DSMC, which is shown instead of pressure determined from the equation of state. For all models, the kinetic stress (center) exhibits a valley, which is smallest for the DSMC case, and largest for EV13. The kinetic heat flux (middle right) has an overshoot in the interfacial region, which is somewhat less pronounced for DSMC.

Of particular interest to understand the non-equilibrium state of the interfacial region are the higher moments which are shown in the last row. The moments $m_{111}$, $R_{11}$ and $\Delta$ vanish in the bulk regions, where the flow is described by NSF. The figures show that the EV26 and EV26R equations match the DSMC curves qualitatively, but not quantitatively, with EV26 again strongly overpredicting the deviation from equilibrium. The moment profiles extend through the Knudsen layer, which thus can be recognized as being significantly wider than the interfacial region defined through the density profile.

It is somewhat disappointing that the regularization EV26R, which in the heat transfer case gives a marked improvement over EV26, does not lead to a similar improvement in the evaporation case.

Fig. 11 shows the same set of curves for a case at lower interfacial temperature $T\left(x_\rho\right)$ with mass flux $J = 0.00035$ and adiabatic vapor. The general behavior is rather similar to that shown in Fig. 10, with a somewhat wider Knudsen layer. The only significant change is the temperature behavior of EV26, which now shows a temperature jump downward ($T_V < T_L$), see the next section for the discussion of this behavior.

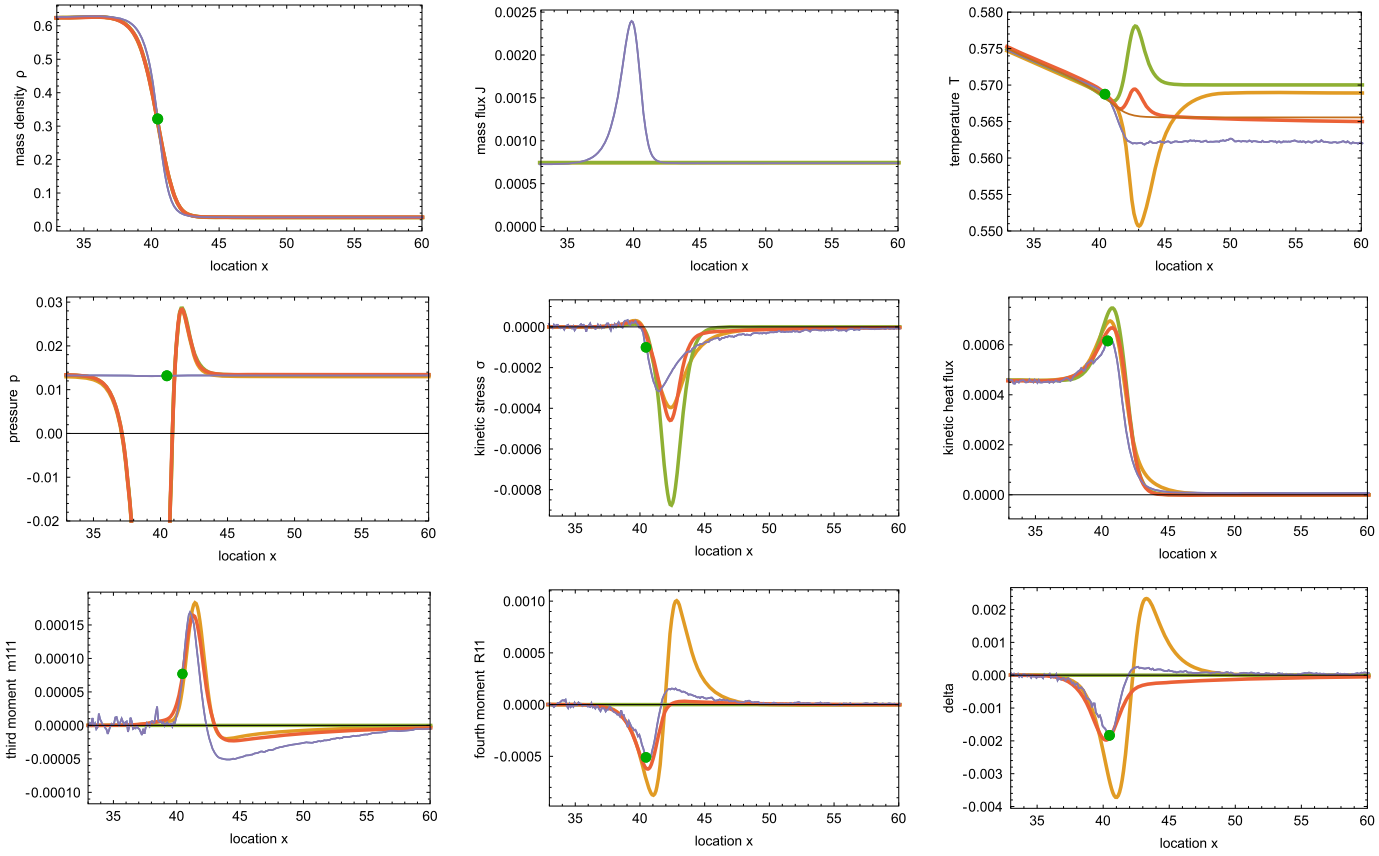


**Fig. 10.** Forced evaporation with adiabatic vapor, for $T\left(x_\rho\right)=0.568$, $J=0.000745$, $q_V=0$. The curves show the values of the EV26 variables and pressure for the interesting interval for various moment sets: EV26 - orange, EV13 - green, EV26R - red, compared to EV-DSMC - purple, NSF ($T$ only) - brown. Green dots indicate the location $x_\rho$ of the steepest density descent. The curves show the values of the EV26 variables (24) and pressure for the interesting interval. Green dots indicate the location $x_\rho$ of the steepest density descent, red dots the location of the temperature minimum.

### 7.2. Evaporation resistivities

For the evaporation case with $q=0$, we can determine the two resistivities

$$\hat{r}_{11}=\frac{p_{\rm sat}\left(T_L\right)}{\sqrt{2\pi RT_L}}\left[\frac{g_L}{RT_L}-\frac{g_V}{RT_V}+h_V\left(\frac{1}{RT_V}-\frac{1}{RT_L}\right)\right]\frac{1}{J}$$
$$\simeq-\left(\frac{1}{\rho_V}-\frac{1}{\rho_L}\right)\frac{p_{\rm sat}\left(T_L\right)}{RT_L}\frac{\Delta p}{\sqrt{2\pi RT_L}}\frac{1}{J} \tag{64}$$

$$\hat{r}_{21}=\frac{p_{\rm sat}\left(T_L\right)}{\sqrt{2\pi RT_L}}T_L\left[\frac{1}{T_V}-\frac{1}{T_L}\right]\frac{1}{J}=-\frac{p_{\rm sat}\left(T_L\right)}{\sqrt{2\pi RT_L}}\frac{\Delta T}{T_L}\frac{1}{J} \tag{65}$$

which again requires extrapolation of bulk curves to the location $x_\rho$.

In classical kinetic theory (10), the resistivity $\hat{r}_{11}$ is linked to the evaporation coefficient, which can thus be estimated as $\psi=\frac{1}{\hat{r}_{11}+0.40044}$. The DSMC data presented in Table 3 suggests values of the evaporation coefficient close to unity, in line with previous investigations [36,77]. For the two temperatures used, $\hat{r}_{11}$ and thus $\psi$, do not vary significantly, while the moment systems predict smaller values for the resistivity at larger temperature. As before, the differences between the values from the $\Delta\left(\frac{g}{RT}\right)$-form and the $\Delta p$-form suggest that for the conditions used linearization around equilibrium might not be allowed.

For the classical ideal gas with full accommodation, the resistivity $\hat{r}_{21}$ is found at a positive value of 0.126 (10). The DSMC data in Table 4 give values that are of the same order, while the various moment systems predict lower, or even negative values, reflecting the visible differences in the curves.

**Table 3**
Resistivity $\hat{r}_{11}$ from extrapolation of microscopic evaporation solutions for DSMC (bold) and EV26R, EV26, EV13 moment equations. Top: Determined from $\Delta\frac{g}{RT}$. Bottom: Determined from $\Delta p$.

| $\hat{r}_{11}\ (\Delta\frac{g}{T})$ | $\theta_L=0.506$ | $\theta_L=0.569$ |
|---|---|---|
| **EV-DSMC** | **0.258** | **0.289** |
| EV26R | 0.524 | 0.350 |
| EV26 | 0.911 | 0.549 |
| EV13 | 0.691 | 0.340 |

| $\hat{r}_{11}\ (\Delta p)$ | $\theta_L=0.506$ | $\theta_L=0.569$ |
|---|---|---|
| **EV-DSMC** | **0.506** | **0.359** |
| EV26R | 0.497 | 0.209 |
| EV26 | 0.846 | 0.394 |
| EV13 | 0.649 | 0.197 |

**Table 4**
Resistivity $\hat{r}_{21}$ from extrapolation of microscopic evaporation solutions for DSMC (bold) and EV26R, EV26, EV13 moment equations.

| $\hat{r}_{21}$ | $\theta_L=0.506$ | $\theta_{bL}=0.568$ |
|---|---|---|
| **EV-DSMC** | **0.132** | **0.100** |
| EV26R | 0.102 | 0.0573 |
| EV26 | 0.0615 | -0.0221 |
| EV13 | -0.0347 | -0.0367 |

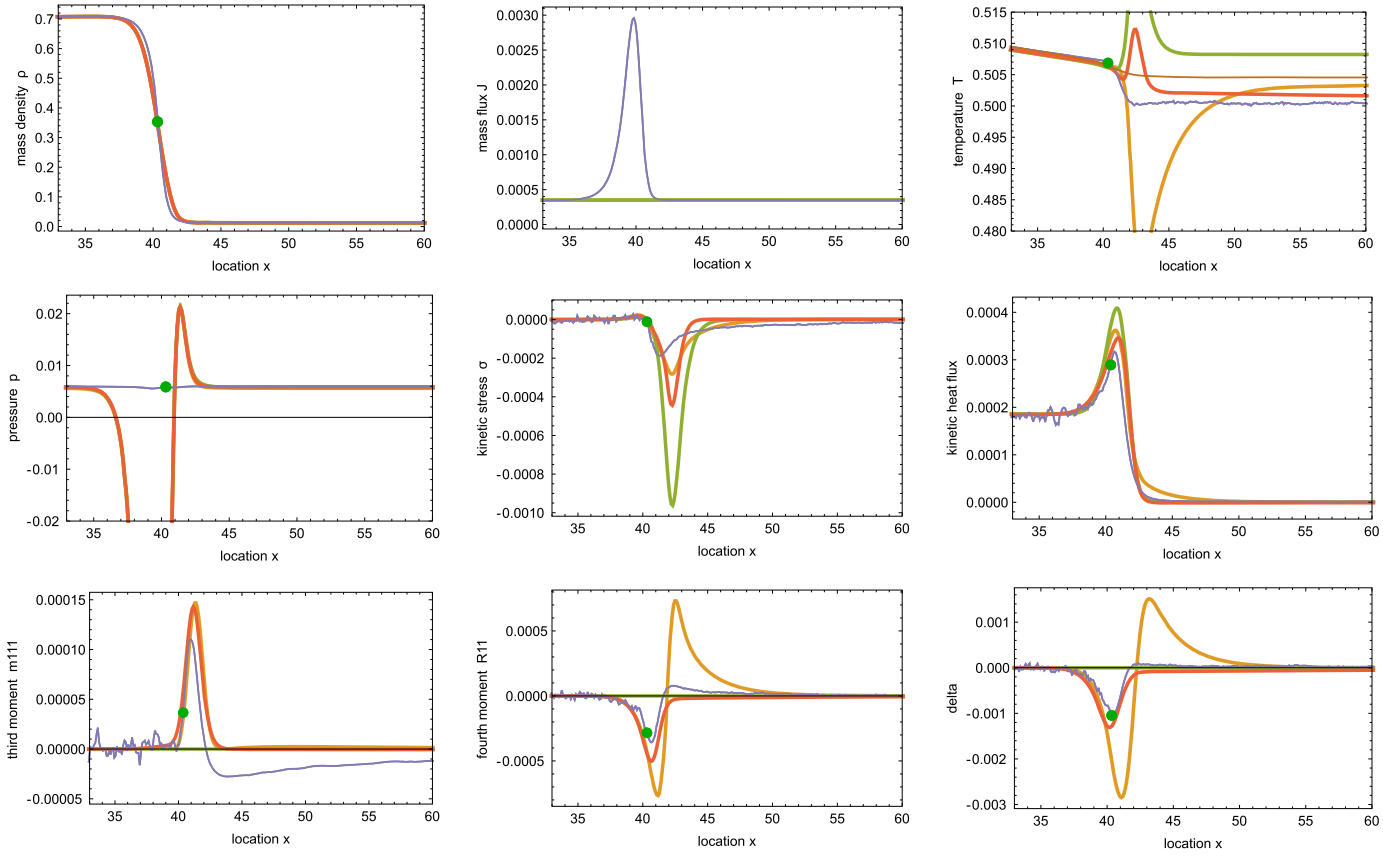


**Fig. 11.** Forced evaporation with adiabatic vapor, for $T\left(x_\rho\right)=0.506$, $J=0.00035$, $q_V=0$. The curves show the values of the EV26 variables and pressure for the interesting interval for various moment sets: EV26 - orange, EV13 - green, EV26R - red, compared to EV-DSMC - purple, NSF ($T$ only) - brown. Green dots indicate the location $x_\rho$ of the steepest density descent.

### 7.3. Discussion of Onsager symmetry

Comparing the data for $\hat{r}_{21}$ in Table 4 to data for $\hat{r}_{12}$ in Table 2, we notice that with these values the resistivity matrix $\hat{r}_{\alpha\beta}$ is not symmetric, but positive definite. With that, the DSMC results appear to not be in full accordance to thermodynamics, which demands a symmetric and positive definite matrix. A possible explanation for this discrepancy is the non-linear behavior of the resistivity matrix. The simulations show nonequilibrium behavior in the interfacial region, with higher moments induced, and Knudsen layers. The related "deformation" of the interface relative to the equilibrium state increases with the degree of non-equilibrium, that is larger mass and heat fluxes could affect the interface behavior, and thus the resistivities.

Referring to Ref. [97] for a deeper analysis, these thoughts suggest that for the 1D processes under consideration, resistivities obey a symmetric relation of the form

$$\hat{r}_{\alpha\beta}=\hat{r}_{\beta\alpha}=\hat{r}_{\alpha\beta}\left(T_s,J,q_V\right)\ , \tag{66}$$

where $T_s$ is a measure for the interface temperature, most often one will use the temperature $T_L$.

Assuming (66) to be valid, the resistivities determined from pure heat transfer and evaporation with adiabatic vapor are, respectively,

$$\hat{r}_{12}\left(T_s,0,q_V\right),\ \hat{r}_{22}\left(T_s,0,q_V\right)\quad;\quad \hat{r}_{21}\left(T_s,J,0\right),\ \hat{r}_{11}\left(T_s,J,0\right) \tag{67}$$

These resistivities are determined at different conditions, and symmetric behavior cannot be expected, $\hat{r}_{12}\left(T_s,0,q_V\right)\neq\hat{r}_{21}\left(T_s,J,0\right)$.

With DSMC limited to stronger deviation from equilibrium, at present we do not have a sufficient amount of reliable DSMC data to fully explore the suggested non-linear behavior that should lead to the relation (66). Further work is necessary, as well as a deeper discussion of the proper thermodynamic development—both are planned for the future. The next section will present non-linear behavior of moment systems.

## 8. EV26/EV26R resistivities

### 8.1. Non-linear behavior in EV26

The deterministic nature of moment equations makes it possible to produce smooth solutions for a wide range of processes, including those close to equilibrium, which are not accessible to DSMC simulations. Since results from the moment systems deviate from those of the full EV equation as found from DSMC we do not present a full evaluation over a wide range of processes, but only show some results to support the above thoughts on non-linear behavior.

As an example, we consider evaporation with adiabatic vapor, with fixed interface temperature $T\left(x_\rho\right)=0.52$ for mass flows $J=\{0.00001,0.0001,0.0005,0.001\}$. Increasing the mass flux $J$, that is for larger evaporation rate, while keeping the interface temperature $T\left(x_\rho\right)$ constant, leads not only to deeper, but also distinctly wider temperature valleys. This can be seen in Fig. 12, which shows kinetic temperature $T=\theta$ in blue and directional kinetic temperatures $T_x=\theta+\frac{\sigma}{\rho},T_y=\theta-\frac{1}{2}\frac{\sigma}{\rho}$, which begin to differ from the location $x_\rho$ onwards into the vapor.

The observed temperature jump must be evaluated over the valley, that is over a much wider region than the jump for pure heat transfer, which is dominated by the steep temperature change around the interface itself as seen, e.g., in Fig. 6. Moreover, the temperature difference

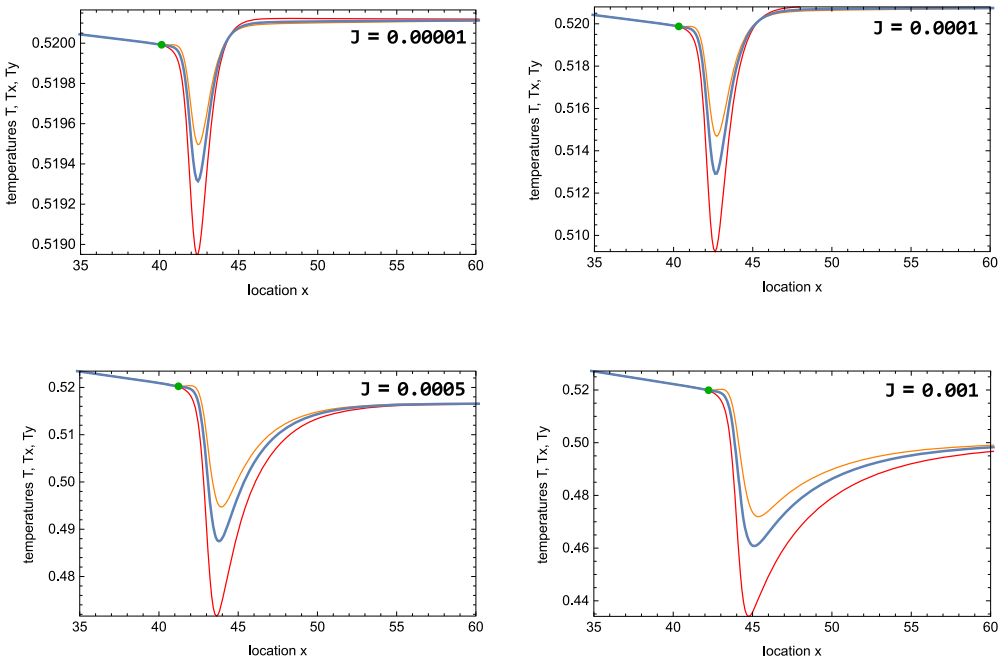


**Fig. 12.** EV26 temperature curves $T$ (blue), $T_x$ (red) and $T_y$ (orange) for $T\left(x_\rho\right)=0.52$, $q_V=0$ for mass flows $J=0.00001$, 0.0001, 0.0005, 0.001.

**Table 5**
Top: Evaporation resistivities $\hat{r}_{11}$ and $\hat{r}_{21}$ from extrapolation of EV26 solutions, for interface temperature $\theta=0.52$ at various mass fluxes. Bottom: heat transfer resistivities $\hat{r}_{12}$ and $\hat{r}_{22}$ from extrapolation of EV26 solutions, for interface temperature $\theta=0.52$ at various heat fluxes.

| evap: EV26 $\theta_L=0.52$ | $\hat{r}_{11}\ (\Delta\frac{g}{T})$ | $\hat{r}_{11}\ (\Delta p)$ | $\hat{r}_{21}$ |
|---|---|---|---|
| $J=1\times10^{-5}$ | 0.884 | 0.884 | -0.109 |
| $J=1\times10^{-4}$ | 0.881 | 0.884 | -0.0760 |
| $J=5\times10^{-4}$ | 0.769 | 0.801 | 0.0597 |
| $J=1\times10^{-3}$ | 0.688 | 0.738 | 0.155 |
| $J=2\times10^{-3}$ | 0.583 | 0.674 | 0.240 |
| **HT: EV26** $\theta_L=0.52$ | $\hat{r}_{12}\ (\Delta\frac{g}{T})$ | $\hat{r}_{12}\ (\Delta p)$ | $\hat{r}_{22}$ |
| $q_V=-1.03\times10^{-5}$ | -0.162 | -0.179 | 1.13 |
| $q_V=-2.05\times10^{-5}$ | -0.161 | -0.186 | 1.13 |
| $q_V=-6.16\times10^{-5}$ | -0.146 | -0.208 | 1.09 |
| $q_V=-1.03\times10^{-4}$ | -0.127 | -0.225 | 1.06 |
| $q_V=-1.99\times10^{-4}$ | -0.0799 | -0.260 | 0.978 |

between $T\left(x_\rho\right)$ and the bulk vapor temperature (which is constant due to $q_V=0$) changes its sign: in the figure we observe $T_V>T\left(x_\rho\right)$ for small mass flows, and $T_V<T\left(x_\rho\right)$ for larger mass flows. This corresponds to a change in sign in the off-diagonal resistivity $\hat{r}_{21}$.

Table 5 (top) shows the corresponding resistivities $\hat{r}_{11}$ and $\hat{r}_{12}$. As before, we compare the values of the resistivities $\hat{r}_{11}$ found from the two expressions in (64), which give identical results for small mass flux (up to $J=10^{-4}$), but different results at larger mass fluxes, where the first order approximation ($\Delta p$) loses validity.

In accordance with Fig. 12, the off-diagonal resistivity $\hat{r}_{21}$ is negative for small mass fluxes, and increases with mass flux towards positive values.

Table 5 (bottom) shows resistivities for heat transfer with $J=0$, for increasing total heat flux $q_V$. Also here, the two expressions for the off-diagonal resistivity $\hat{r}_{12}$ in (62) give similar results for small deviation from equilibrium, and quite different results at larger heat flux, where the expansion into $\Delta p$ loses validity. All values are negative, in agreement with the values for $\hat{r}_{21}$ found from evaporation with low mass flux.

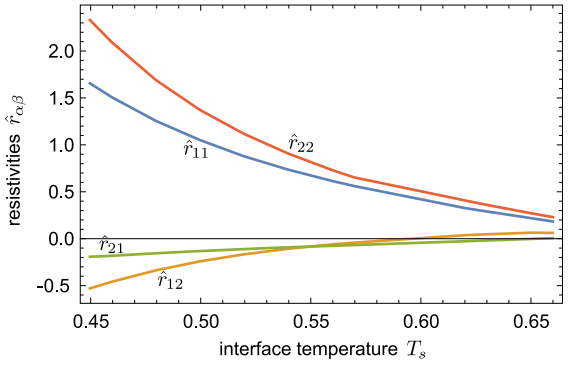


**Fig. 13.** Resistivities over temperature for small deviation from equilibrium ($J=10^{-6}$, $\theta_{bV}-\theta_{bL}=10^{-5}$) for a system of length $L=250$, $L_0=40$, adapted from [48].

The variation of the EV26 resistivities with mass and heat fluxes indicates that resistivities do not only depend on the interface temperature, but also on the degree of nonequilibrium, as stated in Eq. (66).

### 8.2. Temperature behavior in EV26 (linearized)

While the resistivities according to EV26 are not particularly meaningful due to their marked difference from EV-DSMC results, we also show temperature dependence of the four resistivities for close to equilibrium processes in Fig. 13, as adapted from [48]. Under these conditions, all EV26 resistivities change with temperature, with diagonal values $\hat{r}_{11}$ and $\hat{r}_{22}$ decreasing towards the critical point. Off-diagonal resistivities $\hat{r}_{12}$ and $\hat{r}_{21}$ are negative for low temperatures, and then slowly increase with temperature until they change sign towards rather small positive values. While Onsager symmetry is not fully confirmed, both off-diagonal resistivities behave rather similarly, with not too different values.

### 8.3. Non-linear behavior in EV26R

We complement the discussion with Table 6 showing the EV26R counterpart to the EV26 data of Table 5. Here, resistivity $\hat{r}_{11}$ decreases

**Table 6**
Top: Evaporation resistivities $\hat{r}_{11}$ and $\hat{r}_{21}$ from extrapolation of EV26R solutions, for interface temperature $\theta = 0.52$ at various mass fluxes. Bottom: heat transfer resistivities $\hat{r}_{12}$ and $\hat{r}_{22}$ from extrapolation of EV26R solutions, for interface temperature $\theta = 0.52$ at various heat fluxes.

| evap: EV26R $\theta_L = 0.52$ | $\hat{r}_{11}$ $(\Delta \frac{g}{T})$ | $\hat{r}_{11}$ $(\Delta p)$ | $\hat{r}_{21}$ |
|---|---|---|---|
| $J = 1 \times 10^{-5}$ | 0.481 | 0.453 | 0.105 |
| $J = 1 \times 10^{-4}$ | 0.490 | 0.451 | 0.103 |
| $J = 5 \times 10^{-4}$ | 0.494 | 0.461 | 0.104 |
| $J = 1 \times 10^{-3}$ | 0.510 | 0.496 | 0.0920 |
| $J = 2 \times 10^{-3}$ | 0.522 | 0.564 | 0.00743 |
| HT: EV26R $\theta_L = 0.52$ | $\hat{r}_{12}$ $(\Delta \frac{g}{T})$ | $\hat{r}_{12}$ $(\Delta p)$ | $\hat{r}_{22}$ |
| $q_V = -1.82 \times 10^{-5}$ | 0.182 | 0.175 | 0.162 |
| $q_V = -3.66 \times 10^{-5}$ | 0.178 | 0.170 | 0.162 |
| $q_V = -1.11 \times 10^{-4}$ | 0.165 | 0.150 | 0.163 |
| $q_V = -1.86 \times 10^{-4}$ | 0.155 | 0.137 | 0.162 |
| $q_V = -3.70 \times 10^{-4}$ | 0.132 | 0.107 | 0.162 |

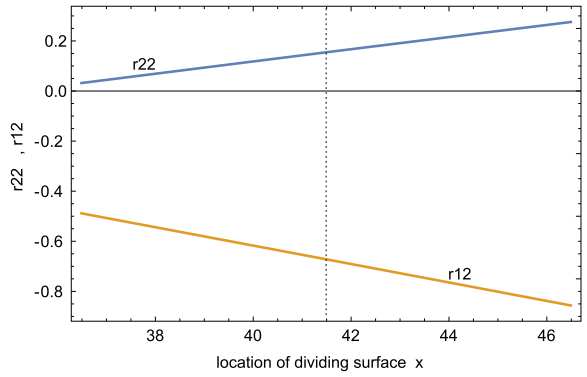


**Fig. 14.** Resistivities $\hat{r}_{12}$ and $\hat{r}_{22}$ in dependence of the chosen location $x_0$ of the dividing surface (jump location). The vertical line indicates the location $x_\rho$ of the steepest density descent. Data for the case with $\theta_{bL} = 0.65$.

slightly with stronger mass flux while $\hat{r}_{22}$ is unaffected by the increase in heat flux. Off-diagonal resistivities $\hat{r}_{12}$ and $\hat{r}_{21}$ are both positive, with values that depend on the strength of the process.

### 8.4. Location ambiguity of resistivities

A second look at Fig. 9 points to an ambiguity in the extrapolation process: Due to the large gradients of temperature and reduced Gibbs free energy on the molecular scale, the size of their jumps $\Delta T$, $\Delta \frac{g}{T}$ depends visibly on the chosen location $x_0$ of the discontinuity (for the heat transfer problem the bulk densities are almost constant, but in evaporation processes liquid density might vary significantly). With this, the values for the resistivities depend noticeably on the location $x_\rho$ of the dividing surface, as shown in Fig. 14. Indeed, a shift of just *one* molecular diameter (recall that $a = 1$ in our scaling!) changes the value for $\hat{r}_{22}$ by about 15% and $\hat{r}_{12}$ by about 5%. Since the bulk gradients and the temperature increase in the interfacial region are proportional to the overall heat flux, the figure remains effectively unaltered for smaller or larger fluxes, that is this is a general problem.

The location of steepest density decent $x_\rho$ appears as a natural choice, in particular since the temperature deviation from the bulk liquid is small until this point, with the steep increase towards the vapor commencing here.

While here is not the place for a deeper analysis, we note that the same issue–dependence of resistivities on location of the dividing surface–occurs in the evaluation of experiments, where bulk data is measured, and extrapolation to the chosen interface location must be used.

## 9. Discussion and outlook

In this contribution, we have studied numerical solutions of the Enskog-Vlasov equation and its EV26 moment system for one-dimensional heat transfer and evaporation processes across diffuse phase interfaces in strong and weak nonequilibrium. Interface resistivities for heat and mass transfer were determined from these results, and compared to classical kinetic theory.

The overall goal of this research is to obtain a better understanding of the interfacial nonequilibrium behavior, which is surprisingly little understood, and generally difficult to ascertain from physical experiments. The simulations resolve the interface, that is the resolution is on the molecular scale. Such a detailed resolution is not practical for simulations of larger systems, hence the interest in finding resistivities for jump interface conditions that are valid on less resolved macroscopic scales. DSMC simulations provide rich insight into the processes studied, but are numerically costly. Just as Molecular Dynamics (MD) simulations, DSMC is somewhat limited to processes in strong nonequilibrium where the results are not affected too much by stochastic noise or transient waves on the small scale.

The EV26 and other moment methods allow for fast deterministic solutions for all processes from weak to strong nonequilibrium. With that, they present themselves as an effective tool to systematically explore interface behavior over a wide range of process conditions. Unfortunately, our results show that the agreement between EV26 and DSMC is somewhat weak, in particular for processes further below the critical point. While the principal behavior of EV26 solutions qualitatively agrees with DSMC, there are significant quantitative differences.

Tests with an ad-hoc regularization (EV26R) show better agreement. Since the regularization results from truncation of a larger moment set, we expect that extended moment systems, with more than 26 moments, will yield better agreement. Deeper consideration of this question is planned for the future.

Higher moments found from DSMC or EV26 have marked contributions in the interfacial area and Knudsen layer. Our results prove that sampling of these higher moments—which vanish in classical hydrodynamics—provides an accessible and meaningful approach to study the non-equilibrium state of the interface.

Interface resistivities are extremely difficult to measure in macroscopic experiments, which are dominated by bulk processes. In contrast, microscopic simulations—with MD, DSMC, or moment systems—center on the interface itself, with only small regions of bulk phases on either side. Resistivities can be found from suitable evaluation based on thermodynamic relations.

While classical kinetic theory models predict constant values for the dimensionless resistivities $\hat{r}_{\alpha\beta}$, our results with DSMC and EV26 show a richer behavior. Specifically, we observed variation of resistivities with temperature and found negative off-diagonal resistivities for some cases. Moreover, the moment results indicate that resistivities depend not only on the interfacial temperature, but also on strength of the nonequilibrium. So far, the latter finding could not be verified from DSMC solutions, which are limited to strong nonequilibrium processes, with sufficiently large heat or mass fluxes.

While the deterministic EV26 moment results, with their smooth curves for all variables, are best suited for the unambigous determination of resistivities, the deviation from DSMC becomes manifest in overly large resistivities, that is too large interface resistance. Tests with other moment systems indicate worse predictions with lower moment number (EV13, EV-NSF), but some improvement from the regularization EV26R.

While inconclusive, our results indicate the need for systematic evaluation of resistivities over a wide range of conditions between weak and strong nonequilibrium, close to and far from critical point. We believe that microscopic simulations with MD, DSMC or moment models are best suited to for this task. Moment equations, with their deterministic solutions for all process conditions, offer an interesting model to exam-

ine and learn about phase interfaces and their resistivities, but higher moment numbers are required.

## CRediT authorship contribution statement

**Henning Struchtrup:** Writing – review & editing, Writing – original draft, Validation, Supervision, Software, Methodology, Investigation, Formal analysis, Conceptualization. **Hamidreza Jahandideh:** Validation, Software. **Arthur Couteau:** Validation, Software. **Aldo Frezzotti:** Writing – review & editing, Writing – original draft, Validation, Software, Methodology, Investigation, Formal analysis, Conceptualization.

## Declaration of competing interest

The authors declare that they have no known competing financial interests or personal relationships that could have appeared to influence the work reported in this paper.

## Data availability

Data will be made available on request.

## Acknowledgements

Part of the results presented were obtained during HS's stimulating long-term visit to the group of Hans Christian Öttinger at ETH Zürich in 2022. HS gratefully acknowledges support from ETH and the Natural Sciences and Engineering Research Council (NSERC) of Canada through Discovery Grant RGPIN-2022-03188.

## References

[1] R. Meland, A. Frezzotti, T. Ytrehus, B. Hafskjold, Nonequilibrium molecular-dynamics simulation of net evaporation and net condensation, and evaluation of the gas-kinetic boundary condition at the interphase, Phys. Fluids 16 (2) (2004) 223–243, https://doi.org/10.1063/1.1630797.
[2] J. Xu, S. Kjelstrup, D. Bedeaux, A. Røsjorde, L. Rekvig, Verification of Onsager's reciprocal relations for evaporation and condensation using non-equilibrium molecular dynamics, J. Colloid Interface Sci. 299 (2006) 452, https://doi.org/10.1016/j.jcis.2006.01.043.
[3] M. Schweizer, H.C. Öttinger, T. Savin, Nonequilibrium thermodynamics of an interface, Phys. Rev. E 93 (2015) 052803, https://doi.org/10.1103/PhysRevE.93.052803.
[4] P. Barbante, A. Frezzotti, A comparison of models for the evaporation of the Lennard-Jones fluid, Eur. J. Mech. B, Fluids 64 (2017) 69–80, https://doi.org/10.1016/j.euromechflu.2017.01.020.
[5] M. Heinen, J. Vrabec, Evaporation sampled by stationary molecular dynamics simulation, J. Chem. Phys. 151 (2019) 044704, https://doi.org/10.1063/1.5111759.
[6] V.V. Zhakhovsky, A.P. Kryukov, V.Yu. Levashov, I.N. Shishkova, S.I. Anisimov, Mass and heat transfer between evaporation and condensation surfaces: atomistic simulation and solution of Boltzmann kinetic equation, Proc. Natl. Acad. Sci. USA 116 (37) (2019) 18209–18217, https://doi.org/10.1073/pnas.1714503115.
[7] S. Homes, M. Heinen, J. Vrabec, J. Fischer, Evaporation driven by conductive heat transport, Mol. Phys. 119 (15-16) (2021) e1836410, https://doi.org/10.1080/00268976.2020.1836410.
[8] A. Frezzotti, P. Barbante, Simulation of shock induced vapor condensation flows in the Lennard-Jones fluid by microscopic and continuum models, Phys. Fluids 32 (12) (2020) 122106, https://doi.org/10.1063/5.0032439.
[9] Ph.M. Rauscher, H.C. Öttinger, J. de Pablo, Nonequilibrium statistical thermodynamics of multicomponent interfaces, Proc. Natl. Acad. Sci. 119 (2022) e2121405119, https://doi.org/10.1073/pnas.2121405119.
[10] S. Kjelstrup, D. Bedeaux, Non-Equilibrium Thermodynamics of Heterogeneous Systems, World Scientific, 2008.
[11] A. Frezzotti, Boundary conditions at the vapor-liquid interface, Phys. Fluids 23 (3) (2011) 030609.
[12] M. Bond, H. Struchtrup, Mean evaporation and condensation coefficients based on energy dependent condensation probability, Phys. Rev. E 70 (2004) 061605, https://doi.org/10.1103/PhysRevE.70.061605.
[13] I. Eames, N. Marr, H. Sabir, The evaporation coefficient of water: a review, Int. J. Heat Mass Transf. 40 (1997) 2963, https://doi.org/10.1016/S0017-9310(96)00339-0.
[14] R. Marek, J. Straub, Analysis of the evaporation coefficient and the condensation coefficient of water, Int. J. Heat Mass Transf. 44 (2001) 39, https://doi.org/10.1016/S0017-9310(00)00086-7.
[15] G. Fang, C.A. Ward, Temperature measured close to the interface of an evaporating liquid, Phys. Rev. E 59 (1999) 417, https://doi.org/10.1103/PhysRevE.59.417.
[16] C.A. Ward, G. Fang, Expression for predicting liquid evaporation flux: statistical rate theory approach, Phys. Rev. E 59 (1999) 429, https://doi.org/10.1103/PhysRevE.59.429.
[17] G. Fang, C.A. Ward, Examination of the statistical rate theory expression for liquid evaporation rates, Phys. Rev. E 59 (1999) 441, https://doi.org/10.1103/PhysRevE.59.441.
[18] C.A. Ward, D. Stanga, Interfacial conditions during evaporation or condensation of water, Phys. Rev. E 64 (2001) 051509, https://doi.org/10.1103/PhysRevE.64.051509.
[19] A.H. Persad, C.A. Ward, Expressions for the evaporation and condensation coefficients in the Hertz-Knudsen relation, Chem. Rev. 116 (2016) 7727–7767, https://doi.org/10.1021/acs.chemrev.5b00511.
[20] M.A. Kazemi, C.A. Ward, Assessment of the statistical rate theory expression for evaporation mass flux, Int. J. Heat Mass Transf. 179 (2021) 121709, https://doi.org/10.1016/j.ijheatmasstransfer.2021.121709.
[21] V.K. Badam, V. Kumar, F. Durst, K. Danov, Experimental and theoretical investigations on interfacial temperature jumps during evaporation, Exp. Therm. Fluid Sci. 32 (2007) 276–292, https://doi.org/10.1016/j.expthermflusci.2007.04.006.
[22] E.Y. Gatapova, I.A. Graur, O.A. Kabov, V.M. Aniskin, M.A. Filipenko, F. Sharipov, L. Tadrist, The temperature jumps at water-air interface during evaporation, Int. J. Heat Mass Transf. 104 (2017) 800–812, https://doi.org/10.1016/j.ijheatmasstransfer.2016.08.111.
[23] L. de Sobrino, On the kinetic theory of a van der Waals gas, Can. J. Phys. 45 (1967) 363–385, https://doi.org/10.1139/p67-035.
[24] M. Grmela, Kinetic equation approach to phase transitions, J. Stat. Phys. 3 (1971) 347–364, https://doi.org/10.1007/BF01011389.
[25] D. Enskog, The numerical calculation of phenomena in fairly dense gases, Ark. Mat. Astron. Fys. 16 (1) (1921).
[26] A.A. Vlasov, Many-Particle Theory and Its Application to Plasma, Gordon and Breach, 1961.
[27] R. Balescu, Equilibrium and Non-Equilibrium Statistical Mechanics, Wiley, 1975.
[28] P. Resibois, M. De Leener, Classical Kinetic Theory of Fluids, Wiley, 1977.
[29] C. Cercignani, Theory and Application of the Boltzmann Equation, Scottish Academic Press, Edinburgh, 1975.
[30] Y. Sone, Kinetic Theory and Fluid Dynamics, Birkhauser, Boston, 2002.
[31] G.M. Kremer, An Introduction to the Boltzmann Equation and Transport Processes in Gases, Springer, Berlin Heidelberg, 2010.
[32] H. Struchtrup, Macroscopic Transport Equations for Rerefied Gas Flows, Springer, Berlin, 2005.
[33] A. Frezzotti, C. Sgarra, Numerical analysis of a shock-wave solution of the Enskog equation obtained via a Monte Carlo method, J. Stat. Phys. 73 (1993) 193–207, https://doi.org/10.1007/BF01052757.
[34] A. Frezzotti, Molecular dynamics and Enskog theory calculation of shock profiles in a dense hard sphere gas, Comput. Math. Appl. 35 (1998) 103–112.
[35] A. Frezzotti, A particle scheme for the numerical solution of the Enskog equation, Phys. Fluids 9 (1997) 1329–1335, https://doi.org/10.1063/1.869247.
[36] A. Frezzotti, L. Gibelli, S. Lorenzani, Mean field kinetic theory description of evaporation of a fluid into vacuum, Phys. Fluids 17 (2005) 012102, https://doi.org/10.1063/1.1824111.
[37] G.A. Bird, Molecular Gas Dynamics and the Direct Simulation of Gas Flows, Oxford University Press, Oxford, 1994.
[38] A. Frezzotti, L. Gibelli, D. Lockerby, J.E. Sprittles, Mean-field kinetic theory approach to evaporation of a binary liquid into vacuum, Phys. Rev. Fluids 3 (5) (2018) 054001, https://doi.org/10.1103/PhysRevFluids.3.054001.
[39] D. Bruno, A. Frezzotti, Dense gas effects in the Rayleigh-Brillouin scattering spectra of $SF_6$, Chem. Phys. Lett. 731 (2019) 136595.
[40] S. Busuioc, L. Gibelli, Mean-field kinetic theory approach to Langmuir evaporation of polyatomic liquids, Phys. Fluids 32 (2020) 093314.
[41] A. Frezzotti, P. Barbante, L. Gibelli, Direct simulation Monte Carlo applications to liquid-vapor flows, Phys. Fluids 31 (6) (2019) 062103, https://doi.org/10.1063/1.5097738.
[42] H. Struchtrup, A. Frezzotti, Twenty-six moment equations for the Enskog–Vlasov equation, J. Fluid Mech. 940 (2022) A40, https://doi.org/10.1017/jfm.2022.98.
[43] D.M. Anderson, G.B. McFadden, A.A. Wheeler, Diffusive-interface methods in fluid mechanics, Annu. Rev. Fluid Mech. 30 (1998) 139–165, https://doi.org/10.1146/annurev.fluid.30.1.139.
[44] H. Grad, On the kinetic theory of rarefied gases, Commun. Pure Appl. Math. 2 (1949) 331–407, https://doi.org/10.1002/cpa.3160020403.
[45] H. Grad, Principles of the kinetic theory of gases, in: S. Flügge (Ed.), Handbuch der Physik XII: Thermodynamik der Gase, Springer, Berlin, 1958.
[46] X. Gu, D. Emerson, A high-order moment approach for capturing non-equilibrium phenomena in the transition regime, J. Fluid Mech. 636 (2009) 177–216, https://doi.org/10.1017/S002211200900768X.
[47] A. Couteau, A continuous model for liquid-vapor transport processes based on Enskog-Vlasov equation: Simulation and Analysis, MASc Thesis, Institut für Fluiddynamik, ETH, Zürich, 2021.
[48] H. Jahandideh, Macroscopic modelling of the phase interface in non-equilibrium evaporation/condensation based on the Enskog-Vlasov equation, MASc Thesis, University of Victoria, 2022.

[49] M.T. Rauter, A. Aasen, S. Kjelstrup, Ø. Wilhelmsen, A comparative study of experiments and theories on steady-state evaporation of water, Chem. Thermodyn. Therm. Anal. 8 (2023) 100091.
[50] H. Struchtrup, Thermodynamics and Energy Conversion, Springer-Verlag, Heidelberg, 2014.
[51] S.R. de Groot, P. Mazur, Non-Equilibrium Thermodynamics, Dover Publications, Inc., New York, 1984.
[52] D. Bedeaux, Nonequilibrium thermodynamics and statistical physics of surfaces, Adv. Chem. Phys. 64 (1986) 47, https://doi.org/10.1002/9780470142882.ch2.
[53] D.C. Venerus, H.C. Öttinger, A Modern Course in Transport Phenomena, Cambridge University Press, Cambridge, UK, 2018.
[54] J.P. Caputa, H. Struchtrup, Interface model for non-equilibrium evaporation, Physica A 390 (2011) 31–42, https://doi.org/10.1016/j.physa.2010.09.019.
[55] H. Hertz, Über die Verdunstung der Flüssigkeiten, insbesondere des Quecksilbers, im luftleeren Raume, Ann. Phys. 253 (10) (1882) 177–193, https://doi.org/10.1002/andp.18822531002.
[56] M. Knudsen, Die maximale Verdampfungsgeschwindigkeit des Quecksilbers, Ann. Phys. 352 (13) (1915) 697–708, https://doi.org/10.1002/andp.19153521306.
[57] R.W. Schrage, A Theoretical Study of Interphase Mass Transfer, Columbia University Press, New York, 1953.
[58] J.W. Cipolla, H. Lang, S.K. Loyalka, Kinetic theory of condensation and evaporation. II, J. Chem. Phys. 61 (1974) 69, https://doi.org/10.1063/1.1681672.
[59] Y.P. Pao, Application of kinetic theory to the problem of evaporation and condensation, Phys. Fluids 14 (1971) 306, https://doi.org/10.1063/1.1693429.
[60] Y.P. Pao, Temperature and density jumps in the kinetic theory of gases and vapors, Phys. Fluids 14 (1971) 1340, https://doi.org/10.1063/1.1693612.
[61] M.N. Kogan, N.K. Makashev, Role of the Knudsen layer in the theory of heterogeneous reactions and in flows with surface reactions, Fluid Dyn. 6 (1971) 913–920, https://doi.org/10.1007/BF01019794.
[62] Y. Sone, Y. Onishi, Kinetic theory of evaporation and condensation – hydrodynamic equation and slip boundary condition, J. Phys. Soc. Jpn. 44 (1978) 1981, https://doi.org/10.1143/JPSJ.44.1981.
[63] D.A. Labuntsov, A.P. Kryukov, Analysis of intensive evaporation and condensation, Int. J. Heat Mass Transf. 22 (1979) 989–1002, https://doi.org/10.1016/0017-9310(79)90172-8.
[64] T. Ytrehus, Molecular flow effects in evaporation and condensation at interfaces, Multiph. Sci. Technol. 9 (3) (1997) 205–327, https://doi.org/10.1615/MultScienTechn.v9.i3.10.
[65] Y. Sone, Kinetic theoretical studies of the half-space problem of evaporation and condensation, Transp. Theory Stat. Phys. 29 (2000) 227–260, https://doi.org/10.1080/00411450008205874.
[66] I.N. Shishkova, A.P. Kryukov, Development of a unified numerical kinetic approach, taking into account many-particle interactions in liquid-vapor systems, Am. J. Phys. Appl. 9 (5) (2021) 116–120, https://doi.org/10.11648/j.ajpa.20210905.13.
[67] M. Kon, K. Kobayashi, M. Watanabe, Method of determining kinetic boundary conditions in net evaporation/condensation, Phys. Fluids 26 (2014) 072003.
[68] D. Bedeaux, S. Kjelstrup, Transfer coefficients for evaporation, Physica A 270 (1999) 413–426, https://doi.org/10.1016/S0378-4371(99)00162-4.
[69] F. Sharipov, Onsager-Casimir reciprocity relations for open gaseous systems at arbitrary rarefaction: I. General theory for single gas, Physica A 203 (1994) 437–456, https://doi.org/10.1016/0378-4371(94)90009-4.
[70] F. Sharipov, Onsager-Casimir reciprocity relations for open gaseous systems at arbitrary rarefraction: II. Application of the theory for single gas, Physica A 203 (1994) 457–485, https://doi.org/10.1016/0378-4371(94)90010-8.
[71] I. Kuscer, M. Robnik, Semi-microscopic description of evaporation and condensation, J. Phys. A, Math. Gen. 13 (1980) 621, https://doi.org/10.1088/0305-4470/13/2/025.
[72] K.W. Kolasinski, Surface Science, 2nd ed., Wiley, Hoboken, 2008.
[73] H. Struchtrup, M. Torrilhon, Regularization of Grad's 13 moment equations: derivation and linear analysis, Phys. Fluids 15 (9) (2003) 2668–2680, https://doi.org/10.1063/1.1597472.
[74] M. Torrilhon, Modeling nonequilibrium gas flow based on moment equations, Annu. Rev. Fluid Mech. 48 (2016) 429–458.
[75] H. Struchtrup, A.F. Beckmann, A.S. Rana, A. Frezzotti, Evaporation boundary conditions for the R13 equations of rarefied gas dynamics, Phys. Fluids 29 (2017) 092004, https://doi.org/10.1063/1.4989570.
[76] A.F. Beckmann, A.S. Rana, M. Torrilhon, H. Struchtrup, Evaporation boundary conditions for the linear R13 equations based on the Onsager theory, Entropy 20 (2018) 680, https://doi.org/10.3390/e20090680.
[77] A. Frezzotti, P. Barbante, L. Gibelli, Direct simulation Monte Carlo applications to liquid-vapor flows, Phys. Fluids 31 (6) (2019) 062103.
[78] G.M. Kremer, E. Rosa Jr., On Enskog's dense gas theory. I. The method of moments for monatomic gases, J. Chem. Phys. 89 (1988) 3240–3247, https://doi.org/10.1063/1.454981.
[79] W. Sutherland, The viscosity of gases and molecular force, Lond. Edinb. Dublin Philos. Mag. J. Sci. 36 (293) (1893) 507–531.
[80] J. Karkheck, G. Stell, Mean field kinetic theories, J. Chem. Phys. 75 (1981) 1475–1487.
[81] H. van Beijeren, M.H. Ernst, The modified Enskog equation, Physica A 68 (1973) 437–456.
[82] P. Resibois, H-theorem for the modified nonlinear Enskog equation, J. Stat. Phys. 19 (6) (1978) 593–609, https://doi.org/10.1007/BF01011771.
[83] S.-Y. Ha, S.E. Noh, New a priori estimate for the Boltzmann–Enskog equation, Nonlinearity 19 (2006) 1219–1232.
[84] J.R. Dorfman, H. van Beijeren, T.R. Kirkpatrick, Contemporary Kinetic Theory of Matter, Cambridge University Press, Cambridge, 2021.
[85] H. Struchtrup, H.C. Öttinger, Thermodynamically admissible 13-moment equations, Phys. Fluids 34 (2022) 017105, https://doi.org/10.1063/5.0078780.
[86] N.F. Carnahan, K.E. Starling, Equation of state for nonattracting rigid spheres, J. Chem. Phys. 51 (1969) 635–636, https://doi.org/10.1063/1.1672048.
[87] D. Bedeaux, E. Johannessen, A. Røsjorde, The nonequilibrium van der Waals square gradient model. (I). The model and its numerical solution, Physica A 330 (2003) 329–353, https://doi.org/10.1016/j.physa.2003.09.042.
[88] E. Johannessen, D. Bedeaux, The nonequilibrium van der Waals square gradient model. (II). Local equilibrium of the Gibbs surface, Physica A 330 (2003) 354–372, https://doi.org/10.1016/j.physa.2003.09.054.
[89] E. Johannessen, D. Bedeaux, The nonequilibrium van der Waals square gradient model. (III). Heat and mass transfer coefficients, Physica A 336 (2004) 252–270, https://doi.org/10.1016/j.physa.2003.12.045.
[90] E.C. Aifantis, J.B. Serrin, The mechanical theory of fluid interfaces and Maxwell's rule, J. Colloid Interface Sci. 96 (1983) 517–529.
[91] H. Struchtrup, A. Frezzotti, Grad's 13 moments approximation for Enskog-Vlasov equation, AIP Conf. Proc. 2132 (2019) 120007, https://doi.org/10.1063/1.5119620.
[92] V. Giovangigli, Kinetic derivation of diffuse-interface fluid models, Phys. Rev. E 102 (2020) 012110, https://doi.org/10.1103/PhysRevE.102.012110.
[93] V. Giovangigli, Kinetic derivation of Cahn-Hilliard fluid models, Phys. Rev. E 104 (2021) 054109, https://doi.org/10.1103/PhysRevE.104.054109.
[94] H. Struchtrup, Stable transport equations for rarefied gases at high orders in the Knudsen number, Phys. Fluids 16 (2004) 3921–3934, https://doi.org/10.1063/1.1782751.
[95] M.P. Allen, D.J. Tildesley, Computer Simulation of Liquids, Clarendon Press, 1989.
[96] T. Savin, K.S. Glavatskiy, S. Kjelstrup, H.C. Öttinger, D. Bedeaux, Local equilibrium of the Gibbs interface in two-phase systems, Europhys. Lett. 97 (2012) 40002, https://doi.org/10.1209/0295-5075/97/40002.
[97] H. Struchtrup, H.C. Öttinger, Nonequilibrium liquid-vapor interfaces: linear and nonlinear descriptions, Phys. Rev. E 108 (2023) 064801, https://doi.org/10.1103/PhysRevE.108.064801.